Vortex dynamics of turbulent energy cascades ⊕

Adrian Parrado Almoguera ⓘ ; Demosthenes Kivotides ✉ ⓘ

Check for updates

View Online   Export Citation

Articles You May Be Interested In

Vortex dynamics of turbulent energy cascades (EP)

View Online   Export Citation   CrossMark

Adrian Parrado Almoguera (iD) and Demosthenes Kivotides[a] (iD)

AFFILIATIONS

Chemical Engineering Department, Strathclyde University, Glasgow G1 1XJ, United Kingdom

[a]Author to whom correspondence should be addressed: demosthenes.kivotides@strath.ac.uk

ABSTRACT

Employing vortex dynamics, we explore the turbulent cascade mechanisms in Schroedinger and Navier–Stokes fluids. While both cascades are driven by vortex instabilities, the ability of Navier–Stokes vortices to stretch and exhibit complex core dynamics significantly affects the resulting turbulence behavior. In dilute Schroedinger turbulence at scales smaller than the intervortex distance, Aarts-de Waele instabilities trigger reconnection-driven Kelvin wave energy cascades, transferring energy from the reconnection scale to smaller scales. At sufficiently long times, these cascades create a high-wavenumber bottleneck before transitioning into a $k^{-5/3}$ local-interaction cascade scaling regime. Energy accumulates in the length scales preceding the bottleneck, triggering partial spectrum equilibration and resulting in a positive scaling exponent there, which differs from the equilibrium value of k^2. At scales larger than the intervortex distance, the spectrum scales as k^2, which is indicative of finite linear impulse in the system. In Navier–Stokes turbulence, the self-stretching of large-core vortices triggers an energy cascade to smaller scales, which is then intensified by the stretching of emergent vortex structures created by Crow or helical vortex line instabilities. The $k^{-5/3}$ scaling arises only once this iterative process has progressed sufficiently to confine flow enstrophy within tubular regions, where the core size becomes a sufficiently small fraction of the overall system size. This confinement causes the vortices to appear quasi-singular when measured on large-scale units. The scaling of the entire-system spectrum is determined by the spectrum of the quasi-singular structures at the culmination of the cascade process, rather than by the cascade process itself.

I. INTRODUCTION

A striking characteristic of turbulence physics is the cascading of energy from large to small scales. This occurs due to nonlinear instabilities, which break down larger eddies into smaller ones, a process first visualized by Richardson. Turbulence cascades are driven by strong inertial effects, with their energy spectra following power-law scalings. The aim of our study is to examine the specific vortex interactions responsible for transferring energy from large to small scales in turbulent flows, and to use these mechanisms to explain the observed spectrum scaling exponents.

In physics, there are two rather different types of turbulent flow. From the practical point of view, turbulence in the Navier–Stokes equation (NSE) is the more important of the two, and historically, turbulence was identified with dissipative, chaotic solutions of the NSE. In the NSE, vortex filament structures have solid-body rotating cores with concentrated vorticity, while their surrounding flow is, to a good approximation, potential with strain but no vorticity. In this work, we present an explanation of the NSE turbulent cascade and its scaling based on the interactions between such vortex filaments.

However, there exists a second, and arguably more fundamental, type of turbulence. This type appears in the Schroedinger equation

(SE), whether in its linear[1] or nonlinear form.[2] Historically, the SE has been known to describe the dynamics of the complex probability of quantum mechanics. However, applying the Madelung transformation reveals a material field interpretation, transforming the Schroedinger equation into a fluid dynamics equation.[3] The material interpretation is employed in finite temperature superfluids[4] to describe the dynamics of the superfluid ground state. In this context, the SE becomes nonlinear and is known as the Gross–Pitaevskii equation. SE fluids are inviscid, *barotropic*, compressible fluids, but, in this work, we exclusively consider their incompressible, large-scale dynamics. In this limit, both the linear and nonlinear Schroedinger equations can be effectively described by the vortex dynamical model, as they feature reconnecting, filamentary vortex solutions characterized by quantized circulation.[1–3] Certainly, the nonlinear term in the Gross–Pitaevskii equation has a significant impact in the compressible regime, as it serves as an additional source of barotropic pressure, complementing the quantum stress and influencing the dynamics of reconnections. However, barotropic pressure becomes irrelevant in the incompressible regime. In the coarse-grained reconnection models employed in vortex dynamics approaches, the subtle effects of nonlinearity at small compressible scales are neglected, focusing exclusively on modeling the dissipative

11 December 2024 14:46:50

action of reconnections and the topological changes they induce. Consequently, a unified vortex dynamical approach to both linear and nonlinear Schroedinger-fluid turbulence becomes feasible. Recently, new SE solvers depicting incompressible SE turbulence have become available.[5] In contrast to the *Eulerian* approach which describes vortices as emergent structures in a material *field*, we instead track SE turbulence vortices in a *Lagrangian* manner, providing an explanation of SE turbulence physics based on their interactions. The key idea that enables us to study these two seemingly unrelated turbulence topics together is that we can numerically model NSE vortices using SE vortices. It is worth noting that our approach, which utilizes Schroedinger filaments as a method for the direct *numerical discretization* of NSE vortices, serves as a complement rather than an overlap to previous efforts aimed at establishing *physical* connections between superfluid and classical turbulence.[6,7]

A key feature of NSE turbulence[8–11] that distinguishes it from other cases of deterministic chaos is the striking organization of its vorticity into predominantly filamentary coherent structures. Interactions between these structures play a key role in the energetics and overall phenomenology of turbulent flows.[12–19] Indeed, to sustain small-scale strain, turbulence requires a continuous energy transfer from large to small scales. The latter is driven by two processes:[8,9,20–22] strain self-amplification, and vortex stretching in the inertial range. The Ref. 22 results suggest an energy-transfer capacity ratio between strain self-amplification and vortex stretching equal to 5/3. Therefore, vortex stretching appears to be a key factor in NSE turbulence energetics, controlling (via the supply of energy to the smallest scales) the generation of turbulent strain and, consequently, the rate of energy dissipation. Certainly, one could argue that vortex stretching is more fundamental than strain self-amplification, as small-scale strain is first generated through vortex stretching in the early stages of the cascade. This is also formally indicated by the well-known formulation of the Navier–Stokes equation expressed entirely in terms of vorticity (i.e., without any strain terms). Thus, from a physical perspective, vortex stretching is a fundamental aspect of the nonlinearity in NSE turbulence, while from an analytical perspective, it plays a critical role in the theory of singularities in the NSE.[23] Conversely, the morphology of SE vortices is highly constrained, allowing only *line* vortices with infinitesimally small cores (the closest natural example of the vortex line concept). All SE vortices have the same quantized circulation, which is not a dynamical variable but depends solely on the material properties of the modeled fluid. While in the NSE, coherent vorticity is embedded within a background of unstructured, lower-intensity vorticity, in the SE, vorticity is zero everywhere except on a set of fractal dimension.[24] Since an NSE vortex filament is essentially a tube filled with vortex lines, and an SE vortex can be thought of as a realization of a vortex line, SE vortices can be used to create discretized models of NSE vortex tubes.[25] Due to their finite core, these NSE vortex models are capable of depicting key NSE phenomena such as core stretching, torsion, and reconnection. The latter is facilitated by the ability of SE vortices to reconnect—an idea first proposed by Feynman[26] and later confirmed by numerical solutions of both linear and nonlinear SE[1,2] and superfluid experiments.[27] This idea establishes a direct link between SE and NSE vorticities, which we will use here to gain a deeper understanding of the self-stretching of NSE filaments and, consequently, the physics of the NSE turbulent cascade and its associated Kolmogorov $k^{-5/3}$ energy spectrum.

Our primary goal is to conduct a comparative study of SE and NSE turbulence, emphasizing the fundamental physical differences between these two types of turbulent phenomena. Our approach to the SE problem is inspired by numerous previous studies,[28–30] which highlight the significant role of vortex reconnections in SE turbulence. We begin by examining the energetics of vortex reconnections. In the next stage, we explore fully developed SE turbulence, aiming to explain its spectra based on the reconnection physics obtained. Conversely, our approach to the NSE problem is motivated by the well-established role of vortex interactions in NSE turbulence.[13–15] We examine the energetics of two distinct NSE vortex configurations and, through numerical simulations, uncover a universal path to turbulence and the Kolmogorov spectrum via vortex instabilities, the formation of emergent vortex structures, and vortex stretching.

Reconnections of SE vortices are a well-studied topic. Svistunov[28] indicated that, due to the singular nature of SE vortices, vortex reconnection in the SE framework should induce Kelvin wave excitations across a continuous range of frequencies. Consequently, this leads to a cascade of energy from reconnection scales toward the smallest excitable scales. The first calculation of the energy cascade spectrum was conducted by evaluating the flow field on an *Eulerian* grid and taking its three-dimensional Fourier transform.[29] This revealed a k^{-1} energy scaling and was followed by additional analytical and numerical studies with both similar and contrasting results (see Ref. 30 for a review). Conversely, Nemirovskii pioneered a *Lagrangian* approach to computing the energy spectrum by using vortex contours and idealizing SE vorticity as a delta function.[31] We continue here this approach and utilize the recent advancements in contour-based energy spectra evaluation presented in Ref. 32. The new energy-spectrum formula derived in Ref. 32 accounts for the fact that numerical vortex dynamics calculations introduce an effective finite core to renormalize the self-interaction singularity in the Biot–Savart law. To ensure consistency, this core is retained in the energy spectrum calculation, replacing the delta function in the approach of Ref. 31. We first apply these new, highly accurate methods alongside parallel algorithms to investigate the energetics of SE vortex reconnections. Following this, we expand our study to the energetics of fully developed SE turbulence cascades, accounting for the effects of chaotic vorticity, multiple reconnections, and interactions between numerous vortices.

In the NSE context, we develop here models of NSE filaments as bundles of SE vortices and use these models to study vortex stretching at high Reynolds numbers and its impact on turbulence physics. In particular, we will explore the formation of the turbulence cascade and the associated Kolmogorov spectrum, focusing on the role of vortex stretching and instability-induced emergent vortex structures. Our results are relevant to other similar in scope investigations, though conducted with different methods. For example, in Ref. 33, an experimental and computational study of vortex rings colliding head-on demonstrated that such strong interactions trigger an (apparently) iterative cascade of instabilities. The latter generate extremely thin vortex sheets that break down into smaller secondary vortex filaments, which then rapidly flatten and further break down into even smaller tertiary filaments. Since no energy spectra were reported, it remains unclear whether this iterative mechanism contributes to the generic turbulence cascade and its Kolmogorov spectrum. The same vortex setup was employed in Ref. 35 to explain the observed clumps of matter along the equatorial ring of Supernova 1987A. A direct connection between

Crow instability and the formation of these lumps was suggested. The analysis was linear, and no energy spectra were reported. Conversely, a theoretical investigation of four NSE vortex rings in a head-on collision[34] observed a $k^{-5/3}$ scaling, though without the iterative mechanism described in Ref. 33 or the detailed resolution of core dynamics that we provide here. Overall, our approach to NSE turbulence aligns with the aforementioned studies, emphasizing the crucial role of interacting vortex structures. We investigate two different configurations: (a) a Hopf link structure, which, similar to Ref. 33, highlights the role of instability-induced emergent structures, and (b) a vortex configuration termed the "vortex collider," developed through experimentation to induce significant vortex stretching and explicitly illustrate dynamic vortex core behavior. Based on our findings, we propose a corresponding interpretation of turbulent cascade processes and Kolmogorov spectra in the NSE.

II. PHYSICAL SYSTEM AND SOLUTION METHODS

The following material has been extensively covered in other publications; therefore, we will only highlight the essential aspects here to ensure completeness of exposition. In vortex-filament dynamics, the velocity vector $v(x)$ of a fluid at *field position* x is given by the Biot–Savart integral over the *filament positions* x':

$$v(x) = -\frac{1}{4\pi} \int \frac{x - x'}{|x - x'|^3} \times \omega(x') dx', \tag{1}$$

where $\omega(x')$ is the fluid vorticity vector. In SE vortices, $\omega(x')$ is represented by a delta function. However, to obtain stable numerical calculations, we assign the filaments a constant core of radius σ which is of the order of the numerical discretization length $\Delta\xi$ (see Refs. 36–39 for details). We have employed both Gaussian and algebraic distributions of vorticity within the numerical core.[37] The self-interaction infinity when $x = x'$ is handled with the method of Schwarz.[40] According to Kelvin's theorem, filaments move with the fluid velocity, so a vortex segment at position z moves with the local flow velocity:

$$\frac{dz}{dt} = v(z). \tag{2}$$

The mathematical model incorporates reconnection induced topological changes.[41] In particular, let $\{z^{k-1}, z^k, z^{k+1}\}$ and $\{z^{l-1}, z^l, z^{l+1}\}$ be any two sequences of discrete vortex point positions (as produced by numerical discretization) along one or two different vortices. The increasing k or l indices are consistent with the vorticity direction along the contours. In numerical calculations, the discrete vortex points are separated by the effective cutoff scale δ_{cf} of vortex contour fluctuations which is of the order of the numerical grid size along the vortices $\Delta\xi$, $\Delta\xi/\alpha < |z^k - z^{k-1}| < \alpha\Delta\xi$. Here, ξ is the arc length parametrization along the vortices, and $\alpha > 1$ is a computational parameter allowing a small variability in the discretization length. In the computations, $\alpha = 1.65$. Next, define the intervortex spacing scale $\delta_{iv} = \sqrt{\mathcal{V}_s/L} = \lambda^{-1/2}$ (with $\mathcal{V}_s$ the system volume, L the vortex tangle length and $\lambda = L/\mathcal{V}_s$ the vortex line density). Accordingly, the reconnection algorithm and the accompanying topological change becomes:

$$\{z^{k-1}, z^k, z^{k+1}\} \wedge \{z^{l-1}, z^l, z^{l+1}\} \wedge (|z^k - z^l| < \beta \min(\Delta\xi, \delta_{iv}))$$
$$\rightarrow \{z^{k-1}, z^k, z^{l+1}\} \wedge \{z^{l-1}, z^l, z^{k+1}\}, \tag{3}$$

where β is a computational parameter, less than unity, that controls reconnection proliferation, with its value depending on the specific

physical context of the investigation. To mimic the loss of kinetic energy into acoustic energy during fully compressible SE vortex reconnections, operation (Physical system and solution methods) is only performed when it leads to vortex length reduction. To the same effect, very small rings with less than four computational points are removed from the system. The dependence of reconnection threshold on the intervortex spacing scale ensures that the production of very dense vortex tangles in the calculation will not lead to the proliferation of spurious reconnections. Equation (2) is an integrodifferential equation that becomes a differential equation following the spatial discretization of the Biot–Savart integral. The differential equation is solved with a third-order accurate Runge–Kutta method. Within the floating point number set $\mathbb{F}$ employed in the algorithms, the distance between 1 and the next larger floating point number is $\epsilon_m = 0.222 \times 10^{-15}$. The smallest and largest numbers that can be represented are 2.2×10^{-308} and 1.8×10^{308} correspondingly. The algorithmic arithmetic employs the round to nearest even rounding method. To investigate long-time equilibration spectra, we applied the Single Input Multiple Data parallelization algorithms from Ref. 42 to vortex dynamics. This approach accelerated the evolution of vortex dynamics by a factor of six and sped up the spectral evaluation by approximately half that amount. Periodic boundary conditions were applied using the minimum image method[43] when appropriate.

III. SCHROEDINGER VORTEX RECONNECTIONS

To investigate SE reconnection energetics, we adopt a configuration (Fig. 1, left) first proposed in Ref. 34. Since SE fluids in nature are superfluids, we use the material parameters of superfluid $He - 4$. Accordingly, the quantum of circulation is $\kappa = 9.97 \times 10^{-4}$ cm^{2}s^{-1} and the physical core radius is $a = 10^{-8}$ cm.

In this setup, four rings with a radius of $R = 0.0415$ cm are arranged in pairs, moving in opposite directions, on two faces of an imaginary cube with side length $l_c = 0.1$cm. Since there is no net linear impulse in the system, the initial low wavenumber energy spectrum presents a k^4 scaling[32] (Fig. 2, right). Similarly with the single ring case,[32] the spectrum shows oscillations superimposed on a k^{-1} scaling at high wavenumbers, before reaching the discretization cutoff (Fig. 2, left). The discretization length along the vortices is $\Delta\xi = 3.906 \times 10^{-4}$ cm, the β parameter is $\beta = 0.1$ and the smoothing core radius is $\sigma = 3.3\Delta\xi$. To resolve better the energy distribution in the small scales, a smaller core radius $\sigma = 0.5\Delta\xi$ was used in spectra calculations. The numerical time step is set so that the fastest Kelvin waves cannot propagate more than $\Delta\xi$ within its duration. The resulting time step is $\Delta t = 6.8 \times 10^{-5}$s. These parameters, along with the floating point number set $\mathbb{F}$ within which the algorithmic arithmetic takes place, ensured stable computations.

As the rings in each pair move toward one another, we observe four simultaneous reconnections, each generating Kelvin waves (Fig. 1, right). These waves propagate from the different reconnections sites and collide at $t = 3.734 \times 10^{-2}$s $= \tau_f$. We will show that τ_f serves as the natural unit for characterizing the system's energetics. The initial reconnections produce two large structures (Fig. 1, right), with the slowest Kelvin waves having wavelengths roughly equal to twice the perimeter of the original rings. We can characterize the slow dynamical processes by the time it takes for these waves to complete a full lap around the structures, $\tau_s = 35$s. Notably, there is nearly a three-order-of-magnitude difference between these two characteristic times.
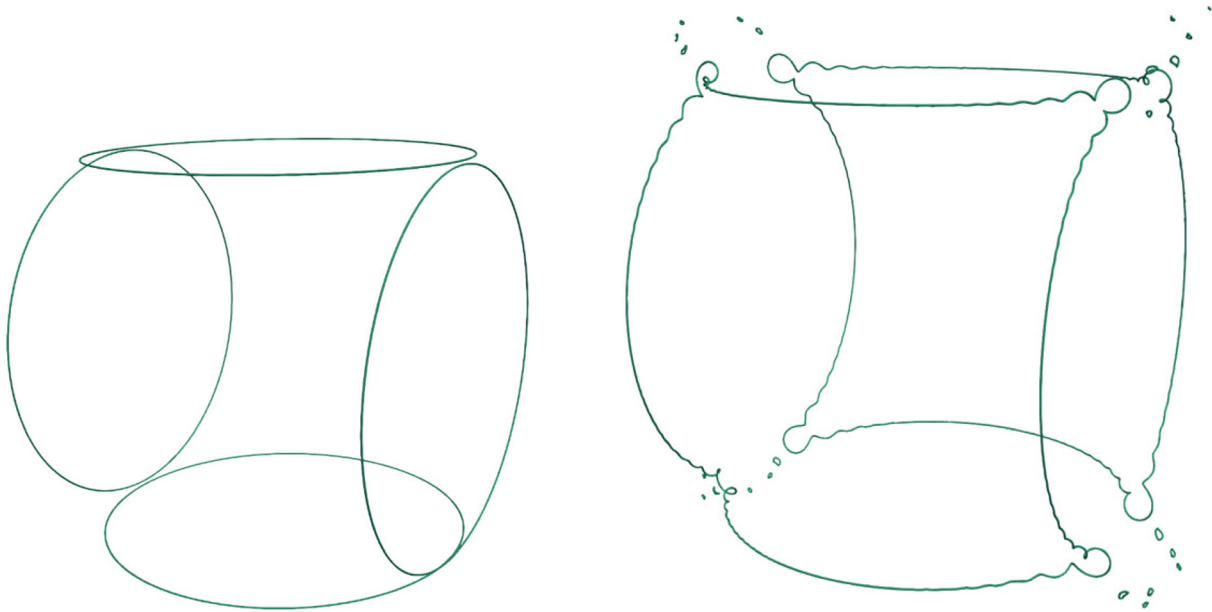
FIG. 1. Initial conditions for the cubic configuration (left). Kelvin waves system after four simultaneous reconnections (right).
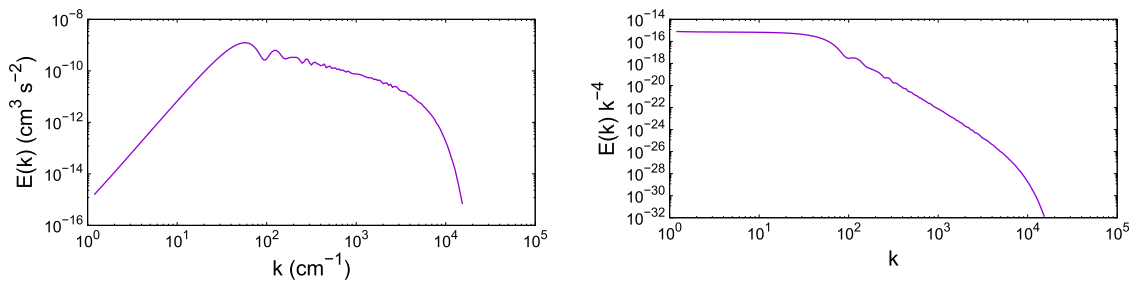

FIG. 2. Energy spectra of the initial conditions of the cubic configuration (left). Same spectra multiplied by k^{-4} to indicate that the initial linear impulse is zero (right).

To analyze our results, we need to determine the timescale within which significant energetic changes occur—that is, to identify the characteristic time of energy transfer via Kelvin waves. To this end, we observe that reconnection-generated helical Kelvin wave configurations do not induce any spectral changes until the collision time τ_f, as the spectra maintain their initial k^{-1} scaling (Fig. 3). As collisional wave interactions build up, the transfer of energy to small scales encounters a high-wavenumber energy-flux bottleneck, leading to an increase in small-scale energy. This causes the spectra to initially evolve toward a flat scaling (Fig. 4) and eventually form a bottleneck bump before transitioning into a $k^{-5/3}$ regime (Fig. 5). Geometrically, wave interactions lead to the formation of highly corrugated vortex contours (Fig. 6). This is evident in the results for $t = 82.82\tau_f$ (Fig. 7, left), where the spectrum's $k^{0.6}$ scaling (Fig. 7, right) approaches the equilibrium value of k^2, indicating *partial spectral equilibration* before the bottleneck.

At the same time, a significant portion of the energy contained in the large vortex structures is "radiated" away as small rings formed by reconnections (Fig. 7, left). This process inhibits direct interactions between the large structures and the smaller waves within them,

leading to energy transfers between the small rings and the rest of the vortex tangle through weaker, nonlocal Biot–Savart interactions. Consequently, in the absence of reconnections, we would expect to observe a stronger spectral equilibration before the bottleneck, while
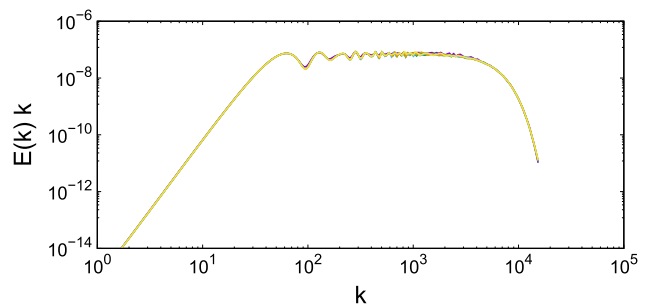

FIG. 3. Compensated energy spectra for the cubic configuration at $t = 0$ (purple), $t = 0.932\tau_f$ (green), $t = 1.005\tau_f$ (blue), $t = 1.096\tau_f$ (orange), and $t = 1.277\tau_f$ (yellow). The plateau demonstrates the k^{-1} scaling. No significant spectral dynamics are observed during the pre-collision phase of Kelvin waves.
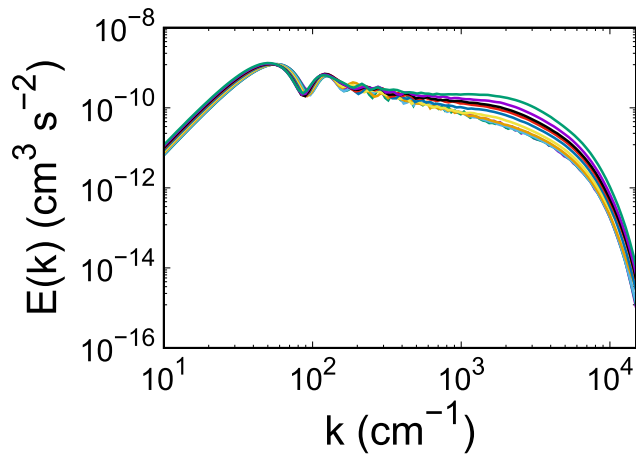
FIG. 4. Evolution of energy spectra for the cubic configuration. From bottom to top, we have $t = 1.097\tau_f$ (green), $t = 2.739\tau_f$ (light blue), $t = 5.484\tau_f$ (orange), $t = 8.044\tau_f$ (yellow), $t = 12.249\tau_f$ (dark blue), $t = 17.185\tau_f$ (red), $t = 20.110\tau_f$ (black), $t = 26.143\tau_f$ (purple), and $t = 36.381\tau_f$ (dark green). A high wavenumber bottleneck is formed.
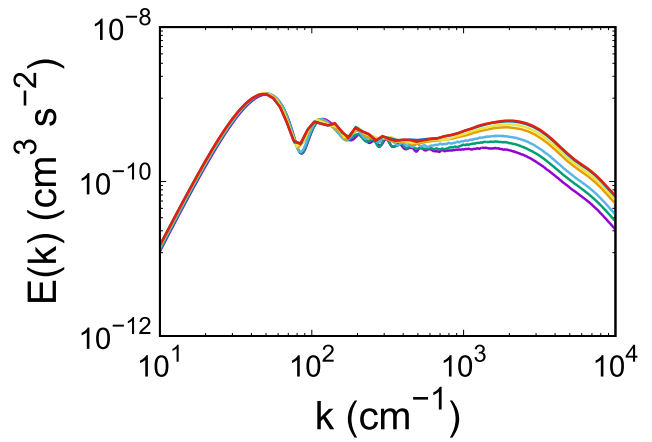
FIG. 5. Evolution of energy spectra for the cubic configuration at $t = 43.51\tau_f$ (purple), $t = 51.01\tau_f$ (green), $t = 58.32\tau_f$ (blue), $t = 71.48\tau_f$ (orange), $t = 76.24\tau_f$ (yellow), $t = 81.54\tau_f$ (dark blue), and $t = 82.82\tau_f$ (red). A post-bottleneck $k^{-5/3}$ spectrum regime is formed.
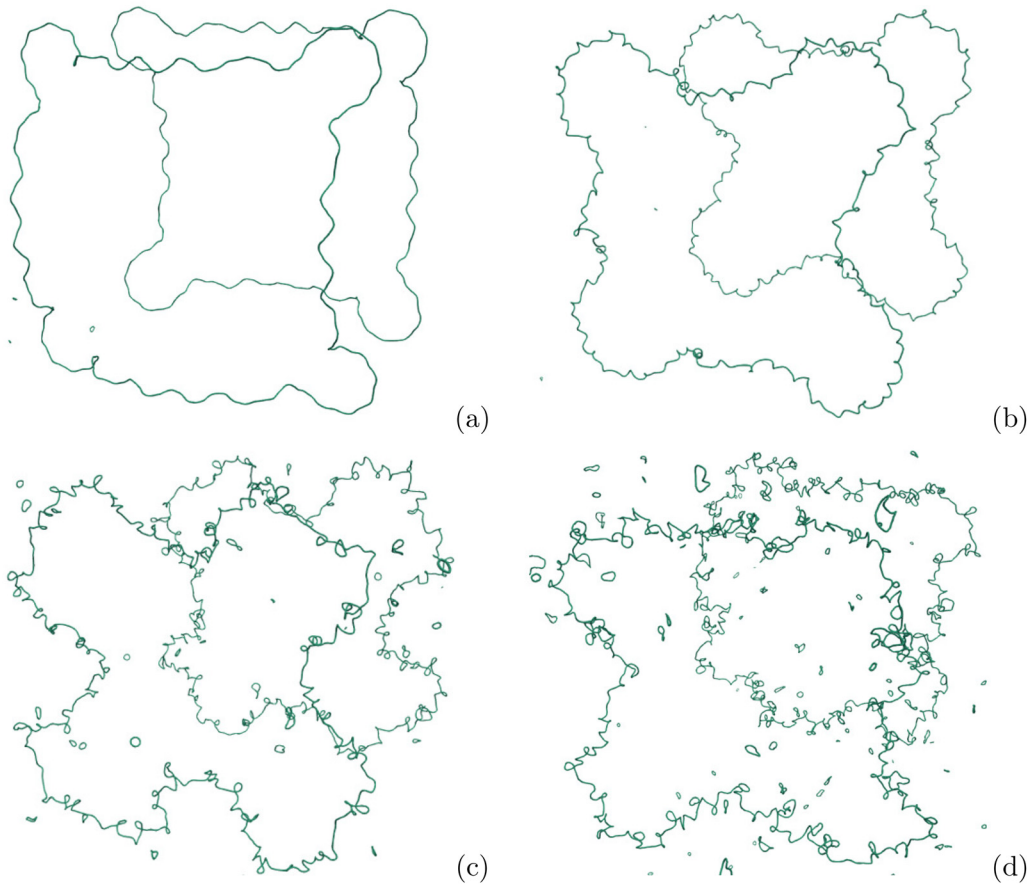

FIG. 6. Cubic configuration vortex tangles at $t = 2.739\tau_f$ (a), $t = 8.044\tau_f$ (b), $t = 20.110\tau_f$ (c), and $t = 36.381\tau_f$ (d).
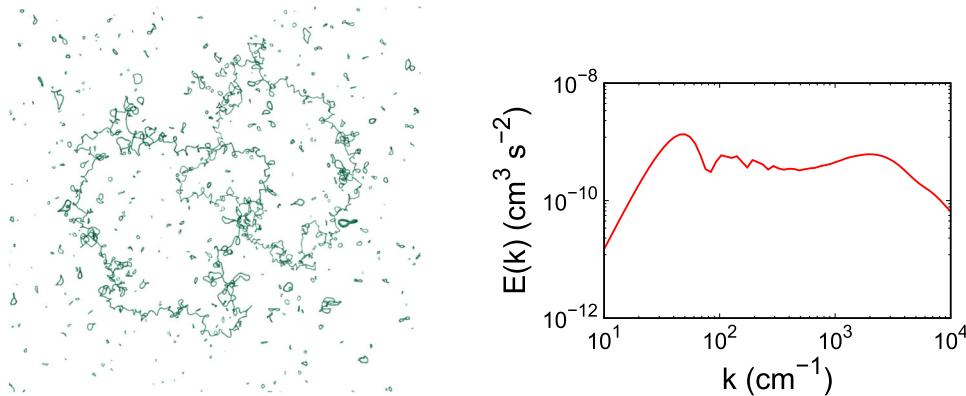
11 December 2024 14:46:50

FIG. 7. Cubic configuration vortex tangle (left) and energy spectra (right) at $t = 82.82\tau_f$ (a). The spectrum follows a $k^{0.6}$ scaling for wavenumbers preceding the bottleneck and a $k^{-5/3}$ scaling beyond it.

drawing similar conclusions otherwise. To test this conjecture, we conducted a calculation where reconnections were disabled after time τ_f. Comparing the vortex tangle configurations at $t = 20.11\tau_f$ shows that, in the absence of reconnections, the filaments become significantly more corrugated (Fig. 8). Furthermore, although the spectra remain similar at $t = 20.11\tau_f$ (Fig. 9, left), a stronger partial equilibration of the pre-bottleneck spectrum is observed at $t = 67.0960\tau_f$ (Fig. 9, right) in the no-reconnections case, thereby confirming our conjecture. Notably, the $k^{-5/3}$ regime is similar in both cases.

Since we now know that the detached rings allow for similar conclusions with the small scales integrated within the large vortex structures, we can exploit the small rings to gain insight into the energetics of the small scales in the system. In particular, we decompose the Biot–Savart velocity v into contributions v_s from small rings with fewer than 20 vortex segments and v_l from larger rings, i.e., $v = v_l + v_s$. We then compute the spectra of the individual contributions (v_l and v_s) as well as the cross or interaction spectra, which offer insights into energy transfers. Shortly after the initial reconnections, the small-ring spectrum exhibits a peak at high wavenumbers and a k^2 regime at the lower ones (Fig. 10, top-left). This is because, unlike the entire system, which

has zero linear vortex impulse and exhibits a k^4 low-wavenumber scaling, there is no reason for the rings created by the reconnections to also have zero linear impulse, therefore, we expect a k^2 far-field regime.[32,44] The interaction spectrum (Fig. 10, top-right) appears noisy, with no clear dominant direction of energy transfer. However, as the system evolves, a dominant energy transfer from large rings to small rings becomes evident (Fig. 10, bottom-right). This occurs near the peak of the large-ring spectrum, where the energy difference between the large rings and small rings is greatest. Notably, the spectra at very large wavelengths reflect only the asymptotic long-distance behavior dictated by the system's net linear impulse, while the actual energy transfer dynamics occur between the spectrum's peak and the cutoff. For this reason (Fig. 10, bottom-left), the small-ring, low-wavenumber k^2 scaling regime beyond the spectrum-peak begins to transition from a linear-impulse signature spectrum to one dominated by Kelvin-wave interactions. The latter become more vigorous at later times (Fig. 11, top), with energy cascading across all scales from large to small wavenumbers. At even longer times, the noisy energy flux at small scales suggests a spectrum quasi-equilibrium (Fig. 11, bottom-right and Fig. 12, top-right), as indicated by an extensive k^2 regime
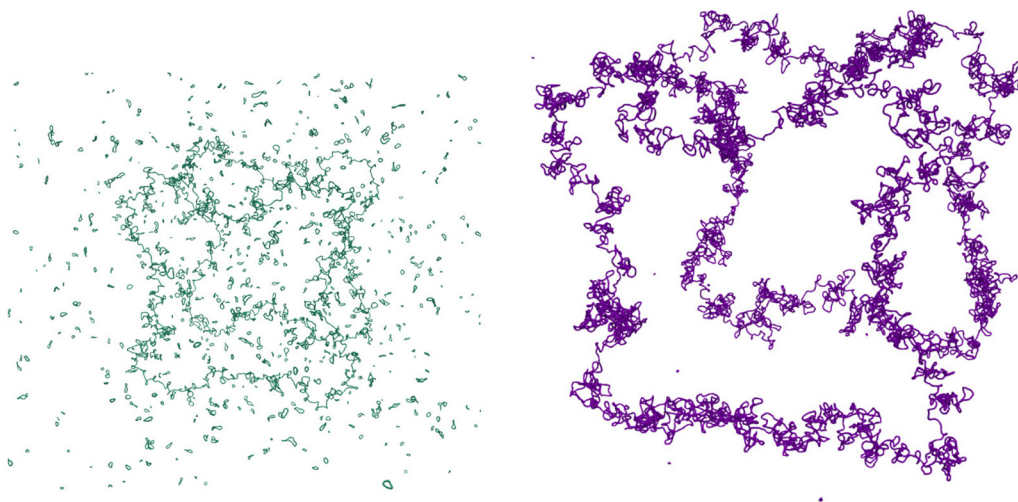

FIG. 8. Cubic configuration vortex tangle at $t = 20.11\tau_f$ when reconnections are allowed (left) and disallowed (right).
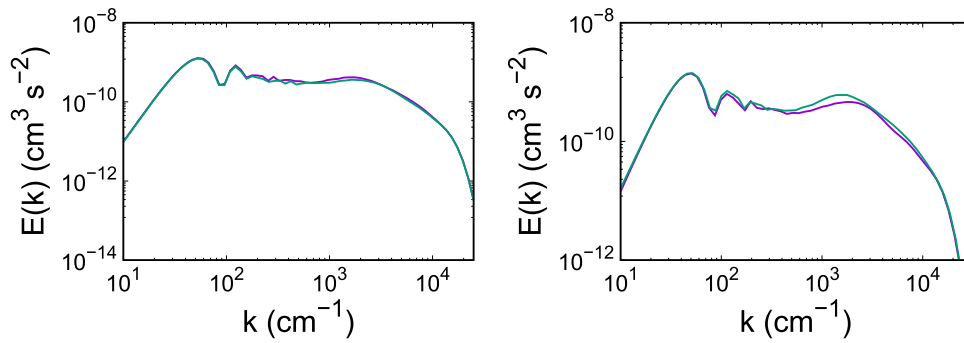
FIG. 9. Cubic configuration energy spectra at $t = 20.11\tau_f$ (left) when reconnections are allowed (green) and disallowed (purple), and at $t = 67.0960\tau_f$ (right) when reconnections are allowed (purple), and disallowed (green).

(Fig. 11, bottom-left and Fig. 12, top-left), resulting from the reshaping of the original linear-impulse scaling. At the longest time (Fig. 12, bottom), the correspondence between the positive scaling exponent in the total spectrum and the small-rings spectrum becomes evident. Notably, all spectra—small-ring, large-ring, total—converge to a high wavenumber $k^{-5/3}$ regime.

These results confirm the interactive nature of the k^2 regime in the small rings, rather than being related to linear impulse. Indeed, we first notice that the area around the bump in the total spectra coincides with the maximum in the small-ring spectra. Furthermore, the same bump in the total spectra is also observed in the calculations without reconnections (Fig. 9). Since, in the no-reconnections case, there are no small rings to produce a nonzero linear-impulse far-field spectrum, the positive slope in this case must result from spectrum equilibration. Thus, we can conclude that the same is true for the interaction-dominated, long-time k^2 regime in the small-ring spectra. This line of

argument is illustrated by observing the temporal evolution of the small-ring spectra (Fig. 13). Clearly, the initial far-field k^2 spectrum ($10^{-1} < k < 2 \times 10^3$, at $t = 16.0884\tau_f$) develops a distinct wiggle that separates (at $t = 82.8188\tau_f$) the far-field spectrum with nonzero impulse ($k < 4$) from an equilibration spectrum dominated by interscale interactions ($20 < k < 2 \times 10^3$). Notably, the onset of the equilibration regime coincides with the emergence of nonzero values in the interaction spectrum (Fig. 12, bottom).

Finally, we can confirm the local nature of the energy flux in the $k^{-5/3}$ regime by observing that the long-time results (Fig. 12, bottom-right) show no interscale energy flux between the large rings and the small rings (those with fewer than 20 segments) in the $k^{-5/3}$ regime. However, we observe such fluxes (Fig. 14, right) when we define the small-rings cutoff as 8 segments. Thus, within the $k^{-5/3}$ regime, rings smaller than 8 segments interact only with rings that are smaller than 20 segments, indicating localized energy-flux processes in that range. It
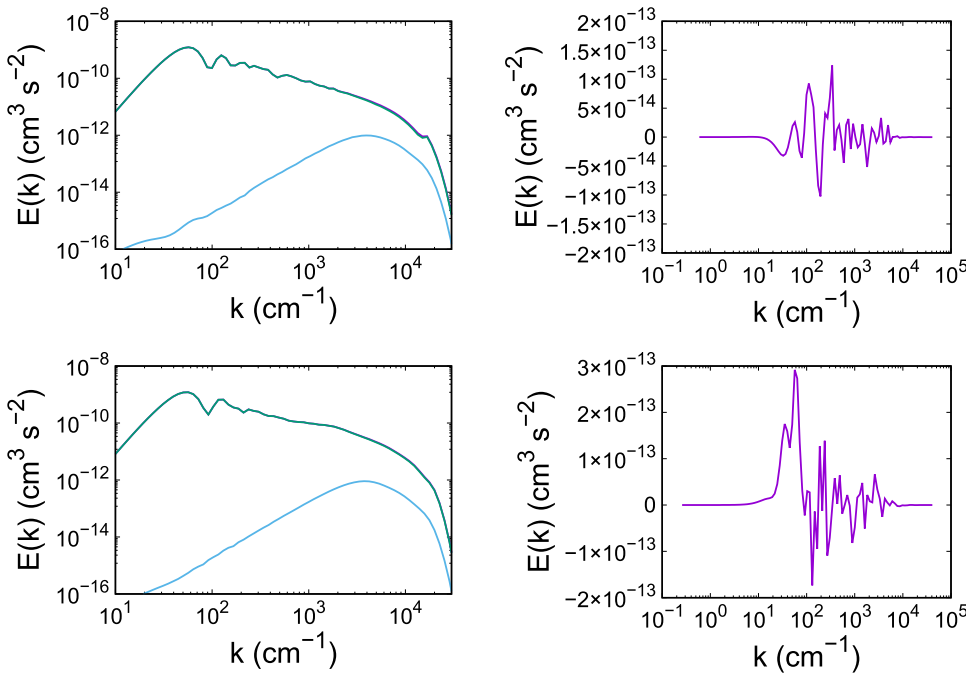

FIG. 10. Cubic configuration: small ring (less than 20 segments), large ring, entire tangle spectra (left) and interaction spectra (right). Top, $t = 2.6874\tau_f$, bottom $t = 10.7317\tau_f$.
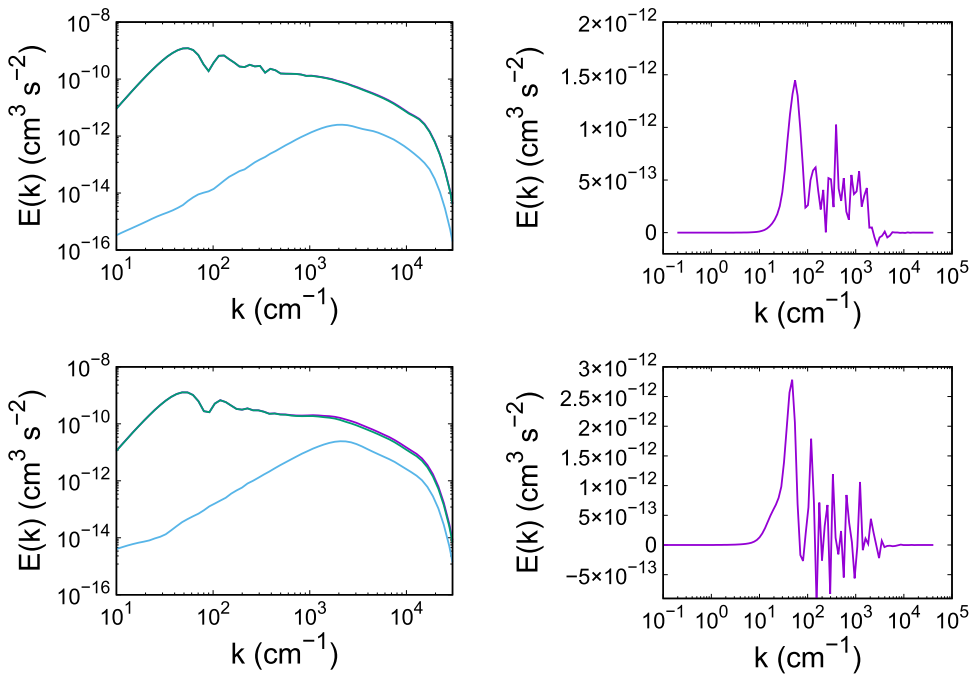
FIG. 11. Cubic configuration: small ring (less than 20 segments), large ring, entire tangle spectra (left) and interaction spectra (right). Top, $t = 16.0884\tau_f$, bottom, $t = 30.5314\tau_f$.

seems that a *portion of the flux* arriving at the bottleneck enters an energy pipeline that transports it to the smaller scales, all the way to the numerical cutoff.

IV. SCHROEDINGER TURBULENCE

Here, we investigate the extent to which SE vortex reconnection contributes to the physics of fully developed SE turbulence. Compared to the cubic case, a key feature of turbulence calculations is the use of periodic boundary conditions, which allow for the definition of a meaningful intervortex distance, encoding the same information as the vortex line density. In this work, we will explore the physics of dilute vortex systems, where the intervortex spacing is much closer to the system size than to the smallest length scales in the computation. Consequently, our calculation offers a high resolution of vortex
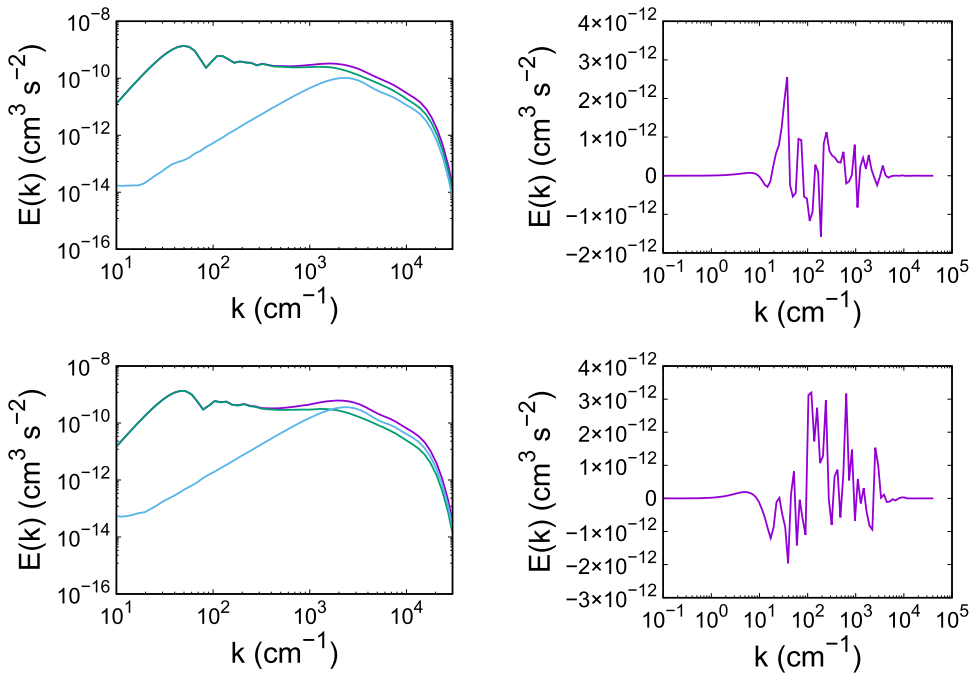

FIG. 12. Cubic configuration: small ring (less than 20 segments), large ring, entire tangle spectra (left) and interaction spectra (right). Top, $t = 51.0076\tau_f$, bottom, $t = 82.8188\tau_f$.
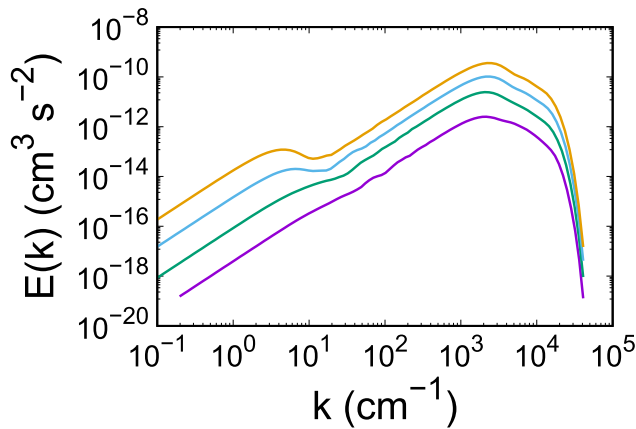
FIG. 13. Evolution of energy spectra of small rings (less than 20 segments) for the cubic configuration at $t = 16.0884\tau_f$ (purple), $t = 30.5314\tau_f$ (green), $t = 51.0076\tau_f$ (blue), and $t = 82.8188\tau_f$ (orange). The initial far-field k^2 spectrum ($10^{-1} < k < 2 \times 10^3$, at $t = 16.0884\tau_f$) develops a distinct wiggle that separates (at $t = 82.8188\tau_f$) the far-field spectrum with nonzero impulse ($k < 4$) from an equilibration spectrum dominated by interscale interactions ($20 < k < 2 \times 10^3$).

FIG. 15. Chaotic configuration vortex tangle at $t = 0$.

processes occurring below the intervortex distance. The initial conditions consist of a system of 100 vortex rings with radii in the range of $[0.015 - 0.0198]$cm (Fig. 15). They are placed within a periodic box with a side length of $b = 0.1$ cm, with random positions and orientations. In this way, the energy is initially concentrated in the large scales, as is typically the case in turbulence. The discretization length along the vortices is $\Delta\xi = 7.8125 \times 10^{-4}$cm, the reconnection parameter is $\beta = 0.3$ and the smoothing core radius is $\sigma = 3.3\Delta\xi$. We selected a higher value of β in this case compared to the reconnections scenario for two reasons: (a) to investigate the impact of this parameter, (b) to verify that the underlying physics remain robust with respect to its choice, and (c) to accelerate the onset of chaos, leading to fully developed turbulence, by increasing the frequency of reconnections. The numerical damping ensured stable calculations, effectively preventing the well-known zig-zag instability in vortex dynamics. For instance, using a smaller core radius of $\sigma = 1.8\Delta\xi$ resulted in unphysical oscillations at the $\Delta\xi$ scale (Fig. 16). To better resolve the energy distribution at small wavelengths, a core radius of $\sigma = 0.25\Delta\xi$ was used in the spectral calculations. The slowest possible Kelvin wave in the system has a wavelength equal to the average vortex-ring length in the initial
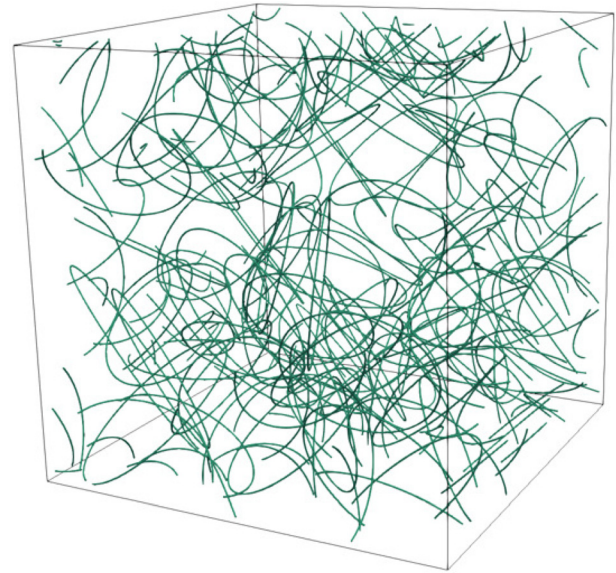
conditions, while the fastest Kelvin wave has wavelength equal to $2\Delta\xi$. To better characterize the dynamics, we define two time scales. The fast timescale, $\tau_f = 0.034$ s, represents the time required for the fastest Kelvin wave to propagate a distance equal to the wavelength of the slowest Kelvin wave in the initial conditions. The slow timescale, $\tau_s = 1.724$ s, represents the time required for the slowest Kelvin wave to propagate a distance equal to its own wavelength. Accordingly, we have $\tau_s/\tau_f \approx 50$.

The energy spectrum in the initial conditions (Fig. 17, left) presents the same k^{-1} scaling as the cubic configuration in the range of scales before the numerical cutoff. However, at large wavelengths, we observe a k^2 scaling (Fig. 17, right), in contrast to the k^4 scaling seen in the reconnection configuration. This difference arises because, in the reconnection case, the net initial vortex impulse is zero, leading to a k^4 spectrum. In contrast, the random vortex-ring arrangement has a nonzero initial vortex impulse, resulting in a k^2 spectrum (see Ref. 32 for detailed discussion).

In comparison with the cubic configuration, we expect that the confined nature of the system and the accompanying higher vortex
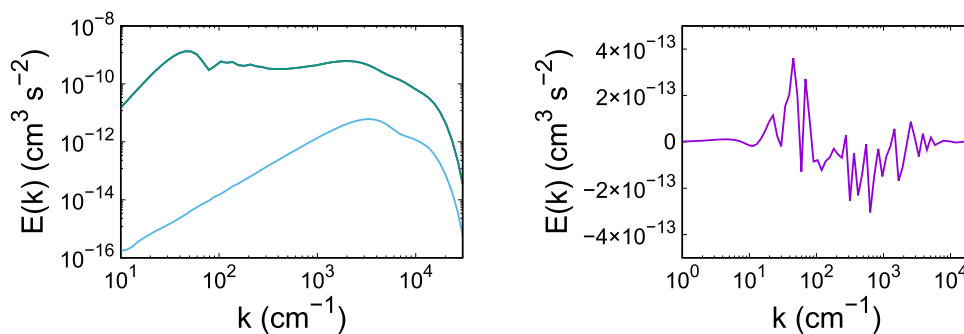

FIG. 14. Cubic configuration: small ring (less than 8 segments), large ring, entire tangle spectra (left) and interaction spectra (right), at $t = 82.8188\tau_f$.
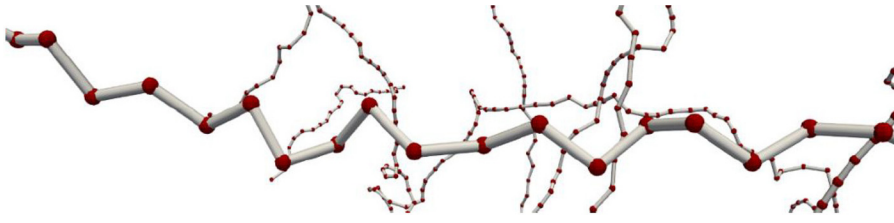
FIG. 16. Example of zig-zag numerical instability.

line densities will have a greater impact on the system energetics. Indeed, a key difference lies in a dynamically significant transient characterized by a high rate of reconnections (Fig. 18). This phenomenon arises from the random initial conditions and the selected value of the reconnection parameter, β. Following this transient phase, the number of reconnections stabilizes into a steady state, increasing linearly with time (Fig. 18). The onset of reconnections generates Kelvin waves cascades along the filaments [Fig. 19(a)] which, for times of the order of τ_f, do not affect the k^{-1} scaling of the initial conditions (Fig. 20, left). This is consistent with the findings in the cubic configuration, where the system evolved over several τ_f times before displaying significant spectral dynamics. For longer times [Figs. 19(b)–19(d)], the high rate of (dissipative) reconnections removes a significant portion of the large-scale energy. As a result, the characteristic bottleneck in the spectra is not observed (Fig. 20, right), as the energy cascading to small scales is reduced compared to the cubic configuration. Accordingly, at $t = 152.083\tau_f$, when large structures remain substantial in the system (Fig. 21, left), we observe a high wavenumber $k^{-5/3}$ regime in both the small-ring and entire tangle spectra (Fig. 22, left). However, the large structures show no signs of an energy bottleneck, while the small rings exhibit a $k^{3/2}$ partial equilibration scaling. To further clarify the role of reconnections, we allow the system to evolve until $t = 22.055\tau_f$, after which we disallow them. At the same time of $t = 152.083\tau_f$ as before, the tangle appears highly corrugated (Fig. 21, right), and the spectrum of the entire vortex tangle exhibits a bottleneck with k^1 scaling (Fig. 22, right). Notably, our vortex system is dilute, as indicated by the relatively low wavenumber corresponding to the intervortex spacing scale (Fig. 22). Above this wavenumber, we observe only the k^2 signature spectrum associated with nonvanishing linear impulse. It has been demonstrated elsewhere[4] that significant spectral dynamics can arise above the intervortex spacing scale, provided there is sufficient vortex line density and excitation.

V. NAVIER–STOKES VORTEX COLLIDER

This configuration was conceived as a vortex dynamics analog to the well-known elementary particle colliders. The goal is to use colliding NSE vortices to confine high enstrophy and intense vortex stretching processes within small regions of space. We have applied the method from Refs. 37 and 45 to discretize NSE tubes as bundles of SE vortices.

In particular, we arranged 49 SE vortex rings within a cylindrical NSE filament to achieve a circulation $\Gamma = 0.049$ cm^{2}s^{-1}. The diameter of the vortex ring at the centerline is $D_{cl} = 0.083$ cm, and the tube-core radius is $R_{tc} = 0.0083$ cm. The discretization length along the SE vortices is $\Delta\xi = 2.371 \times 10^{-3}$cm, and the numerical core radius is $\sigma = 1.1\Delta\xi$. The numerical core radius used in the calculations of the spectra took values in the range between $0.25\Delta\xi$ and $1.1\Delta\xi$. The reconnection parameter was set to $\beta = 0.1$. We have arranged six such tubes in the following configuration (Fig. 23): two NSE tubes are set up to collide with each other in each direction. The distance between the planes that contain their centerlines is $0.4D_{cl}$. Moreover, to prevent head-on collisions and introduce more complex vortex dynamics, we offset the centers of their centerlines along directions perpendicular to the collision axis. For instance, if the collision direction is along the x-axis, the offsets are applied in the y and z directions. These offsets are each $0.2D_{cl}$, and because they have opposite signs for the bundles in a colliding pair, the total offset along the two directions perpendicular to bundle motion is $0.4D_{cl}$. The initial system configuration is confined within a cubic box with dimensions $l_b = 0.1$ cm. The vortex dynamics take place in an unbounded domain. Based on the diameter of the centerline vortex ring and bundle circulation, we compute a characteristic time $\tau_c = 0.083^2/(49 \times 9.97 \times 10^{-4}) = 0.141$ s. The offsets and initial distances are crucial in determining the type of vortex dynamics observed in the system. The final choices resulted in vigorous vortex stretching and core dynamics over sufficient time periods to support our conclusions.
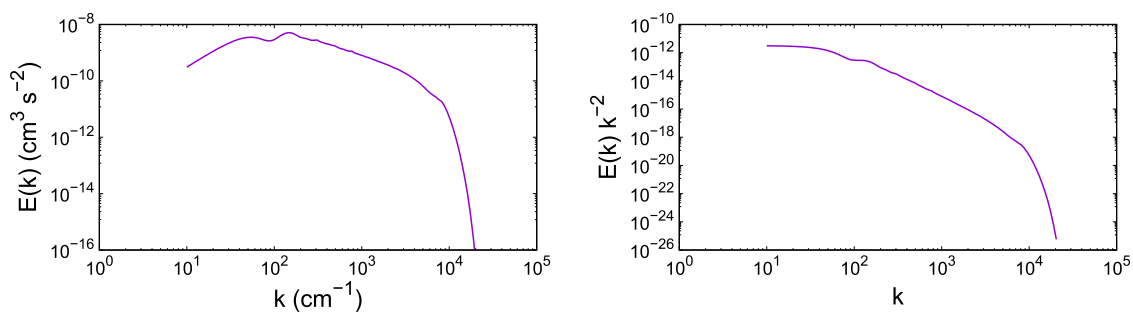
FIG. 17. Energy spectra of the chaotic tangle configuration at $t = 0$ (left) and compensated energy spectra at $t = 0$ (right), highlighting the nonzero linear impulse of the initial conditions.
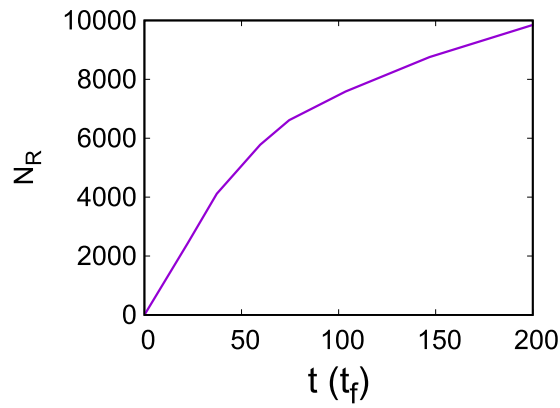
FIG. 18. Chaotic configuration: Number of reconnections N_R vs time (in τ_f units).

The initial conditions spectra (Fig. 24) exhibit a k^{-4} scaling at low wavenumbers, which is a consequence of the zero linear impulse at $t = 0$. There is no evidence of $k^{-5/3}$ scaling. During the initial stages of evolution, vortex stretching occurs, leading to energy transfer to smaller scales, but without the establishment of a Kolmogorov regime (Fig. 25). The vortices continue to stretch until at $t = 0.1486\tau_c$ (Fig. 26), the smallest cores in the system reach typical radii of approximately $r_c = 0.00258$ cm (Fig. 27, left), resulting in a ratio $l_b/r_c \approx 40$. The corresponding wavenumber $k_c \approx 380$ marks the end of a brief $k^{-5/3}$ range (Fig. 28). Moreover, there is evidence of core sheetification processes (Fig. 27, right) consistent with findings from other studies using Navier–Stokes solvers, such as Refs. 46 and 47. As the system evolves, vortex stretching intensifies, and by time $t = 0.4457\tau_c$, due to well-documented instabilities,[12,48,49] the vortex lines within the cores become helical, implying that stretching is now accompanied by core torsion and changes in core size (Fig. 29). Subsequently, at time $t = 0.5942\tau_c$, the helical vortex lines form emergent vortex structures
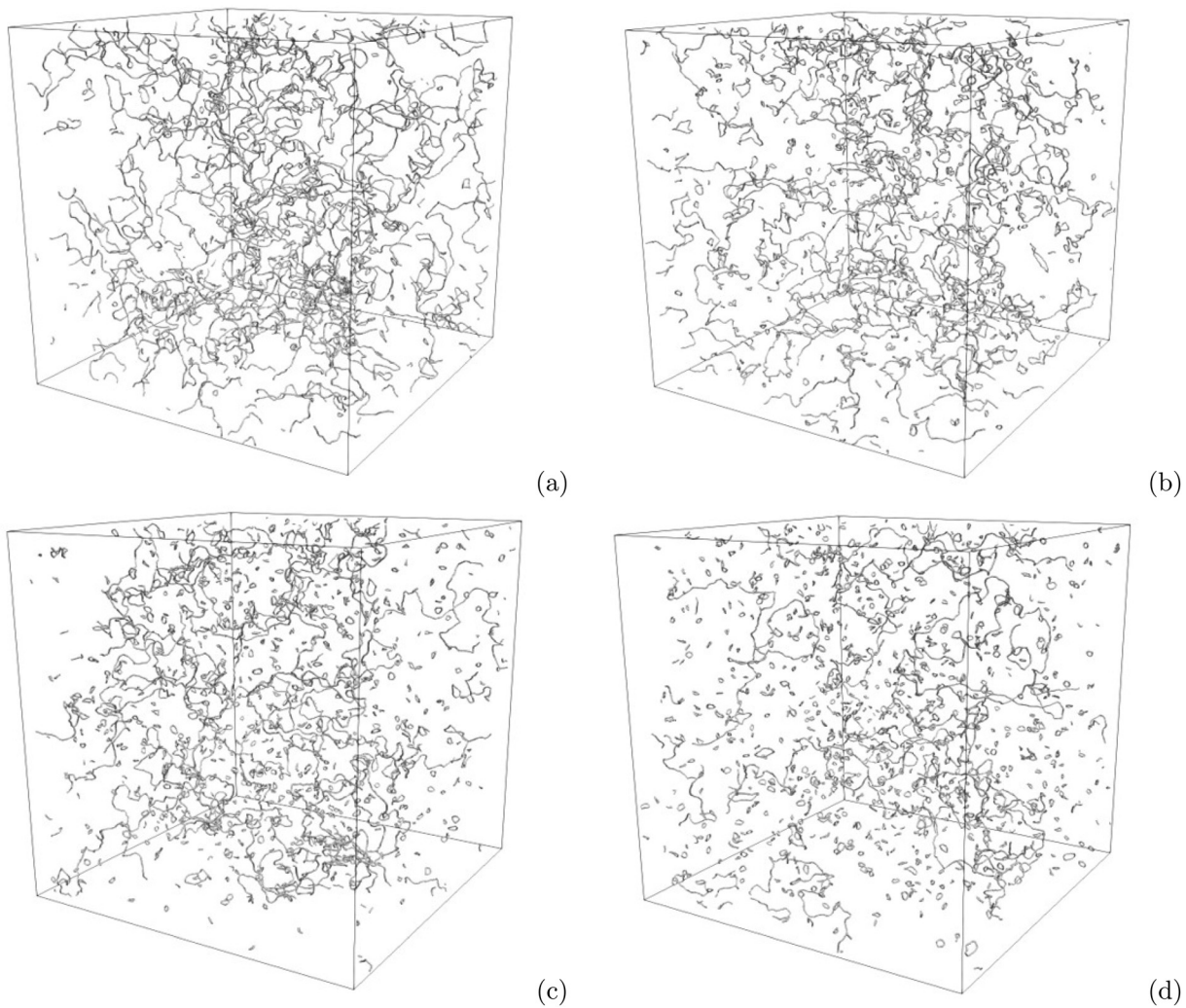

FIG. 19. Cubic configuration vortex tangles at $t = 22.05\tau_f$ (a), $t = 36.755\tau_f$ (b), $t = 73.515\tau_f$ (c), and $t = 144.82\tau_f$ (d).
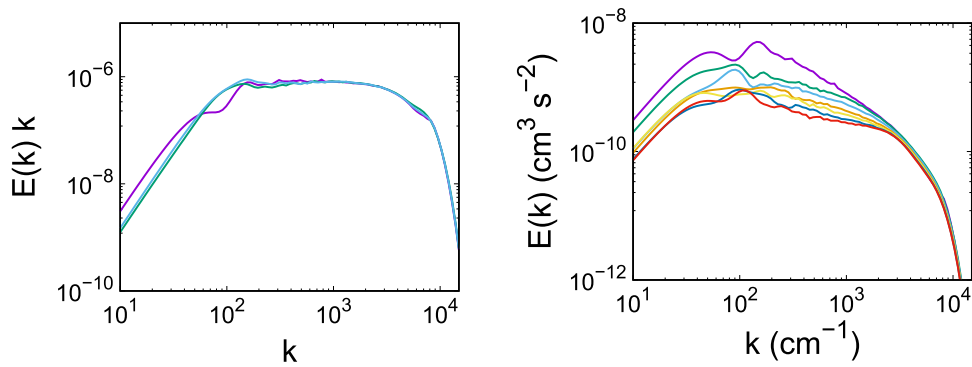
FIG. 20. Energy spectra of the chaotic configuration. Left: compensated spectra at $t = 0$ (purple), $t = 0.7\tau_f$ (blue), and $t = 2.2\tau_f$ (green). Up until times on the order of τ_f, the generation and propagation of Kelvin waves do not affect the spectrum. Right: $t = 0$, $t = 22.05\tau_f$, $t = 36.755\tau_f$, $t = 58.8\tau_f$, $t = 73.515\tau_f$, $t = 102.185\tau_f$, $t = 144.82\tau_f$ (top to bottom).
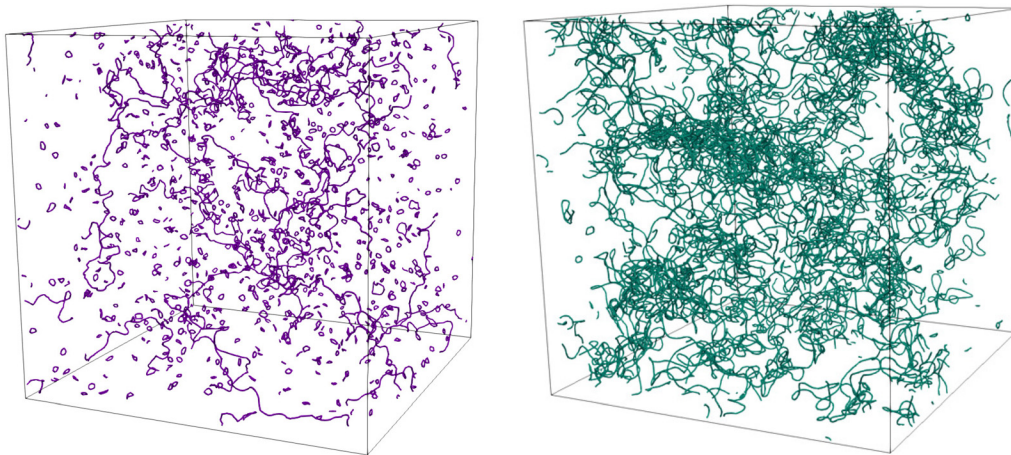

FIG. 21. Chaotic configuration vortex tangle at $t = 152.083\tau_f$ with reconnections allowed (left) and reconnections disallowed (right).
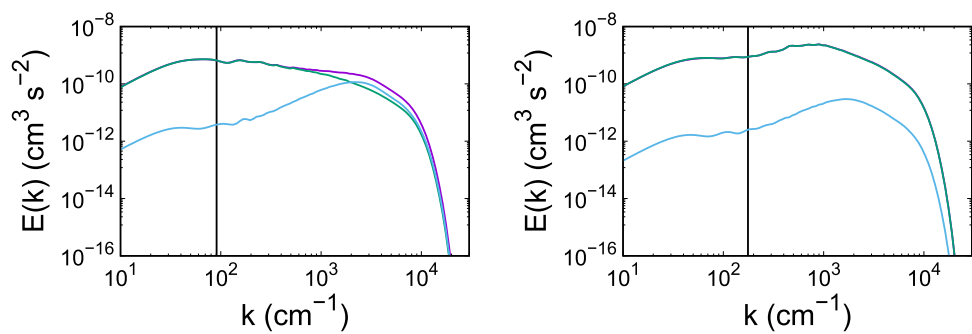

FIG. 22. Chaotic configuration: Energy spectra for small rings (less than 20 segments, blue), large rings (green), and entire vortex tangle (purple). On the left, reconnections are allowed—on the right, reconnections are disallowed. The vertical line indicates the intervortex spacing scale.

(Fig. 30) whose stretching extends the $k^{-5/3}$ scaling regime toward higher wavenumbers (Fig. 31). These higher wavenumbers correspond to the sizes of the smaller structures emerging in the system (Fig. 32). Remarkably, the observed stretched filaments, originally arcs in the

initial configuration, are straightened by extensional strain. This suggests that the observed stretching process may be characteristic of curved-vortex stretching in actual turbulent flows. These results support an alternative interpretation of Kolmogorov's $k^{-5/3}$ law: rather

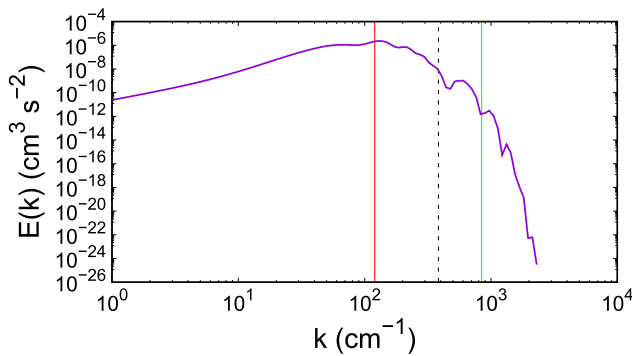**FIG. 23.** Initial conditions of collider bundle configuration.

FIG. 24. Initial energy spectrum of collider bundle configuration. The red line corresponds to the bundle core radius, the green line to the intervortex distance within the core, and the dashed black line to the diagnostics core radius.
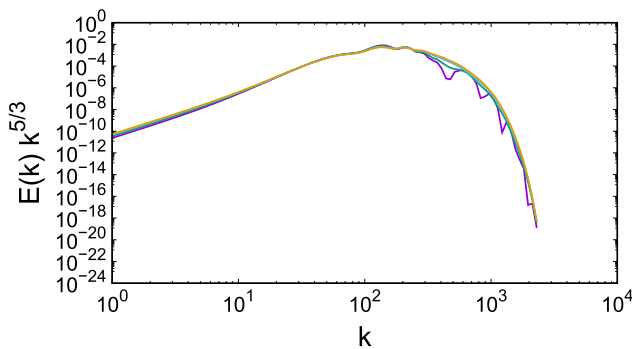

FIG. 25. Compensated energy spectra of collider bundle configuration at $t = 0$ (purple), $t = 0.046\tau_c$ (green), $t = 0.089\tau_c$ (blue), and $t = 0.118\tau_c$ (yellow).
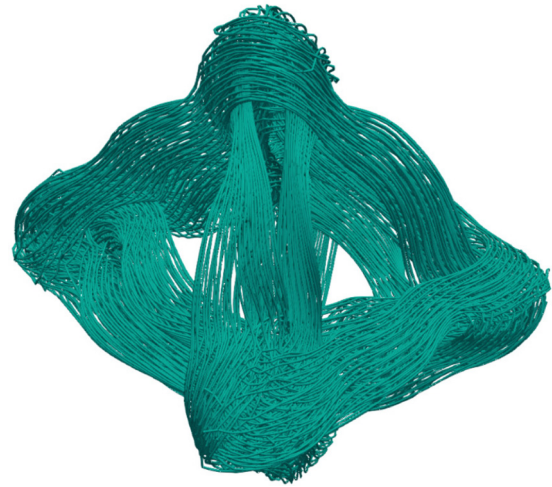

FIG. 26. Collider bundle configuration at $t = 0.1486\tau_c$.

than being directly related to energy transfer between scales, it may instead be connected to the formation of high-intensity enstrophy structures as the end product of energy cascading events. Due to their quasi-singular nature, these structures exert influence across a broad range of wavenumbers. Their broad spectral footprint, coupled with their high signal-energy, likely causes the high-frequency scaling to "leak" into the lower frequency range, thereby affecting the entire spectrum.

To test this idea, we evolve the initial conditions *kinematically*, by streching the initial bundles without altering the geometry or inner structure of the vortex tubes, while preserving the total filament volume (Fig. 33). Although the initial spectrum shows no evidence of a Kolmogorov regime (Fig. 34, purple line), the situation changes as the kinematic stretching of the tubes progresses. When the core radius reaches 0.0062 cm (Fig. 34, green line), a $k^{-5/3}$ regime emerges in the spectra, which approximately ends at wavenumber $k = 160$, corresponding to the tube radius. At this stage, the ratio of system size over bundle radius is $l_b/r_c = 32$, which aligns well with the value of 40 observed in the vortex collider case. Similarly (Fig. 34, blue line), when the core radius reaches 0.00415 cm, the Kolmogorov regime terminates at the corresponding wavenumber, approximately $k = 240$. In all cases, the Kolmogorov scaling begins at the core size and extends toward lower wavenumbers. Since these spectra are generated kinematically and are not part of any specific vortex dynamical evolution, it is reasonable to conclude that the Kolmogorov spectrum reflects the imprint of quasi-singular structures on the inertial range of turbulence. Therefore, it is linked to the final outcome of the cascade process (quasi-singular vorticity) rather than the energy-transferring turbulent instabilities in the inertial range.

Furthermore, we observe that vortex line torsion is not a necessary condition for the emergence of a Kolmogorov spectrum. Its physical role lies in forming emergent vortex structures, whose subsequent stretching forms quasi-singular structures at smaller scales, thereby extending the Kolmogorov spectrum to higher wavenumbers. It is important to note that the smallest vortex cores, with the highest enstrophy values, correspond to the smallest scales of turbulence (just before the viscous cutoff). As a result, the $k^{-5/3}$ spectrum always
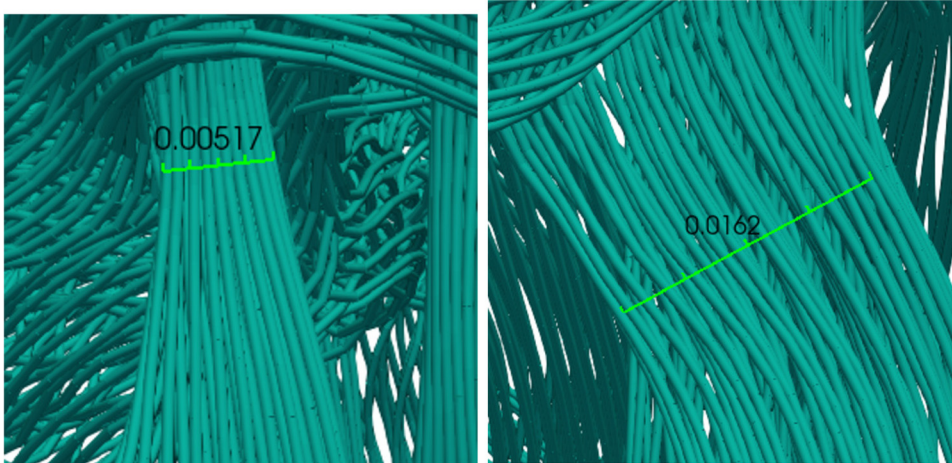
FIG. 27. Collider bundle configuration at $t = 0.1486\tau_c$. Example of core thinning on the left, and sheetification on the right.
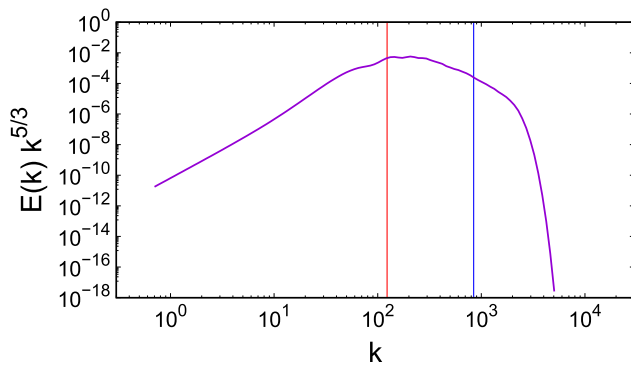

FIG. 28. Compensated energy spectrum of collider bundle configuration at $t = 0.1486\tau_c$. The red line corresponds to half of the axial distance between pairs of colliding bundle centerlines in the initial configuration, and the purple line to the diagnostics core radius.

begins at the end of the turbulent inertial range, rather than in the middle of it. Additionally, since the tubes are perfectly cylindrical in the kinematic case, whereas they exhibit sheetification processes in the dynamical case, the kinematic calculation suggests that the key factor for Kolmogorov scaling is the confinement of enstrophy at small scales, rather than the specific geometry of these vorticity structures. Moreover, since the spectrum of vortex sheets follows a k^{-2} scaling,[32] which is absent in our results, it implies that *possibly* both the confinement of enstrophy into quasi-singular structures and the closed circular topology of these structures at large scales are crucial. These findings point to the need for a thorough topological analysis of NSE turbulent vorticity.

VI. NAVIER–STOKES VORTEX LINK

The vortex Hopf link problem has been well-studied with NSE solvers in the context of vortex reconnection and topological change studies. Our purpose here is to employ our approach of modeling NSE
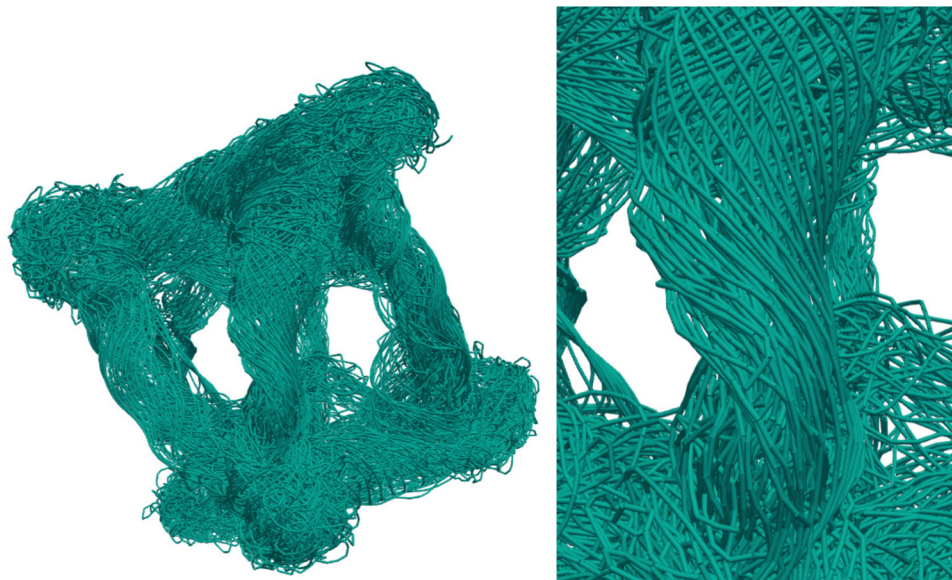

FIG. 29. Collider bundle configuration at $t = 0.4457\tau_c$. Whole system on the left, and example of vortex line torsion on the right.
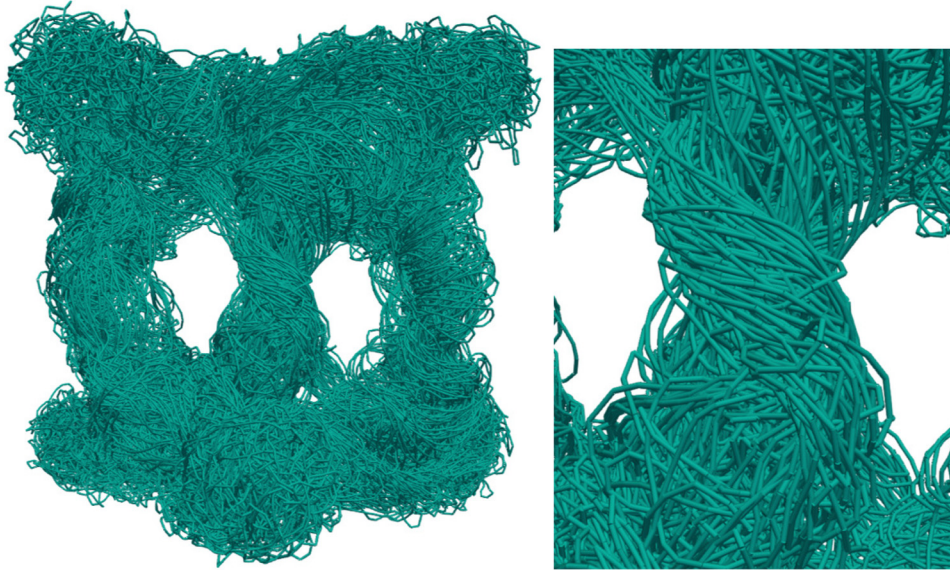
FIG. 30. Collider bundle configuration at $t = 0.5942\tau_c$. Whole system on the left, and example of an emergent vortex structure on the right.

tubes via SE vortices to test our ideas about the role of vortex stretching and instabilities in turbulence, as these were formed by reflecting upon the results of the vortex collider configuration. To highlight the effects of vortex configuration as we transition from the collider to the link cases, we use identical bundles, computational parameters, and characteristic times for the link as in the vortex collider case. The link is formed by having the centerlines of the one ring pass through the center of the centerline of the other (Fig. 35, left).

For times less than the characteristic time, the evolution of the system (Fig. 35, middle and Fig. 35, right) shows similar features with NSE solutions.[25,51,52] On the route to reconnection, the bundles *stretch each other* creating two straight segments of antiparallel vorticity (Fig. 35, right). Similarly with the vortex collider, the corresponding spectra (Fig. 36) show a transfer of energy to smaller scales but there is no discernible alteration of the initial spectrum as far as the
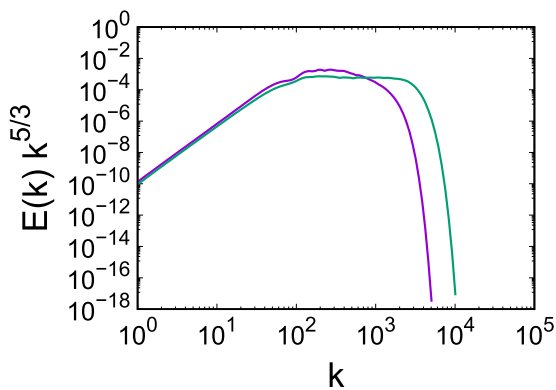

FIG. 31. Compensated energy spectrum of collider bundle configurations at $t = 0.4457\tau_c$ (purple) and $t = 0.5942\tau_c$ (green).
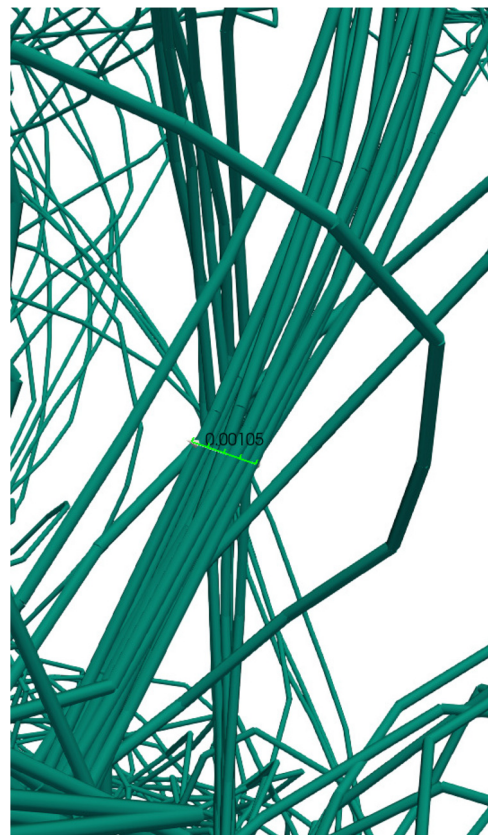
FIG. 32. Collider bundle configuration. Example of thin vortex structure at $t = 0.5942\tau_c$.
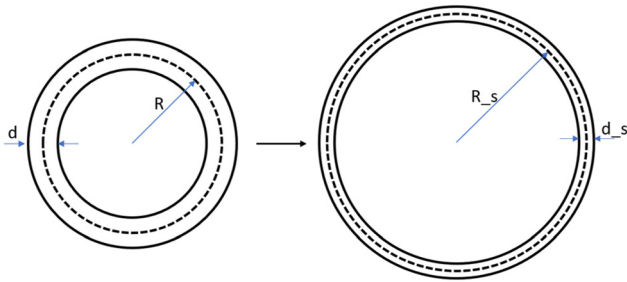
FIG. 33. Kinematic vortex stretching. The initial bundle radius R and core diameter d become R_s and d_s after the application of isochoric kinematic stretching.
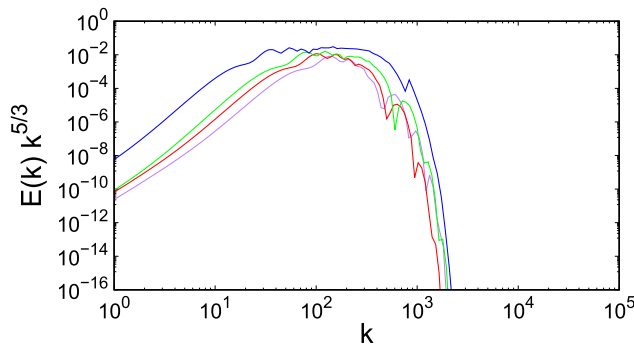

FIG. 34. Kinematic vortex stretching. Compensated energy spectra for original core size (purple), 15% core reduction (red), 25% core reduction (green), and 50% core reduction (blue) showing a growing $k^{-5/3}$ regime.

wavenumbers close to its peak are concerned. As already mentioned, the antiparallel vortices are the setting of the Crow instability which appears, in the beginning, as wavy vortex lines (Fig. 37, left) which form Λ like instabilities that tend to wraparound the antiparallel vortex cores (Fig. 37, right). The corresponding spectra (Fig. 38) show this dynamic by lowering the energy of the large scales and indicating the initial stages of a $k^{-5/3}$ regime formation. Although the energy cascade to smaller scales is clearly demonstrated in the results, there is no comparable demonstration of a Kolmogorov regime. This is because the link configuration is not as conducive to stretching phenomena as the vortex collider. Unlike the collider case, where helical vortex lines
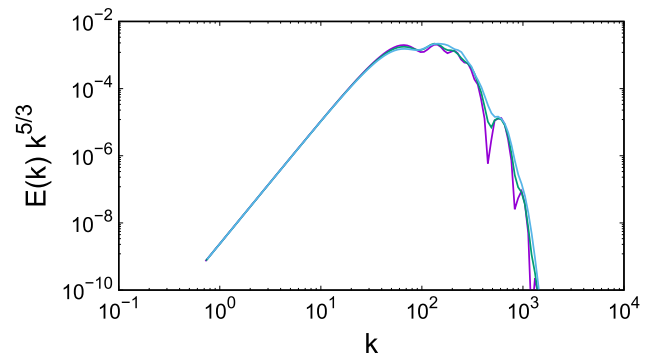

FIG. 36. Bundle link configuration. Compensated energy spectra at times $t = 0$ (purple), $t = 0.4454\tau_c$ (green), and $t = 0.7426\tau_c$ (blue). A transfer of energy from large to small scales is noticable.

bunched together and formed strong, self-stretching emergent structures, such effects are absent in the link configuration, although the vortex bundles are identical in both cases.

The stretching deficit caused by different initial configurations can, however, be compensated by enhancing the inertial effects in the system—specifically, by increasing the circulation of the bundles in the link case compared to the collider case. Therefore, we increased the number of SE vortex rings in the bundles from 49 to 81, raising the circulation to $0.0807\,\mathrm{cm^2 s^{-1}}$. The corresponding characteristic time is now $\tau_c = 0.0853\,\mathrm{s}$. We accounted for the increased vortex density within the tubes by adjusting the numerical core used in the spectral computations to a value of $\sigma = 0.5\Delta\xi$ value. With increased inertial effects in the system (Fig. 39), and given the higher vortex-line density, the Crow instability forms emergent bundles of vortex lines (Fig. 40). Due to their increased inertia and finite core size, these bundles can undergo significant self-stretching, similar to what was observed in the vortex collider case. A comparison of the spectra for the cases with 49 and 81 vortices (Fig. 41) reveals that the higher inertia case displays a well-defined Kolmogorov plateau, analogous to what is observed in the vortex collider case.

VII. CONCLUSION

The results suggest two distinct energy cascade mechanisms for SE and NSE turbulence. While both cascades are driven by vortex instabilities, the capacity of NSE vortices to stretch and display intricate
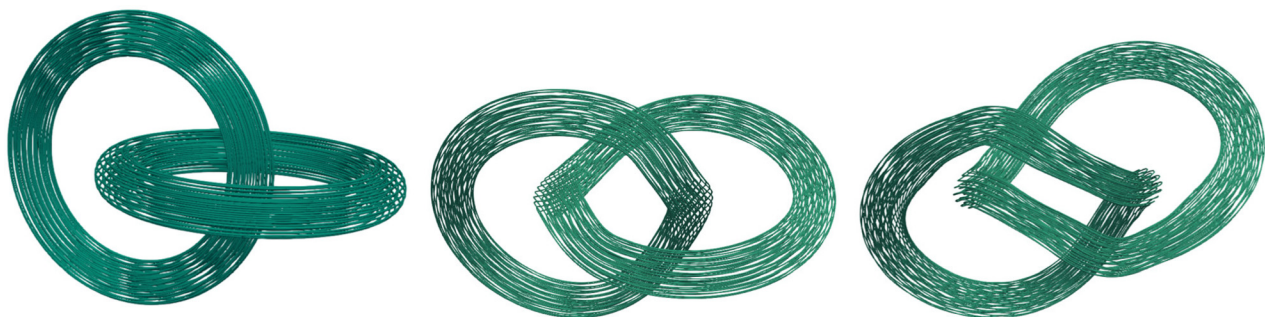

FIG. 35. Bundle link configuration vortex tangles at $t = 0$ (left), $t = 0.4454\tau_c$ (middle), and $t = 0.7426\tau_c$ (right).

FIG. 37. Bundle link configuration vortex tangles at $t = 1.0397\tau_c$ (left) and $t = 1.1879\tau_c$ (right).

core dynamics drastically influences the corresponding turbulence behavior. In SE turbulence the primary instability is the Aarts-de Waele instability,[50] which drives neighboring filaments toward reconnection. In contrast, in NSE turbulence, key roles are played by the Crow and helical vortex line instabilities. The latter instability is responsible for both the initial phase, during which vortex lines form a helical structure, and a subsequent phase, where the instability of this helical structure leads to the formation of emergent vortex structures. In SE turbulence, the Kelvin waves induced by the Aarts-de Waele instability are the sole mechanism for energy transfer from the reconnection scale to the smallest scales in SE turbulence. Indeed, since SE vortices are modeled as true vortex lines, SE vortex stretching merely increases filament length without the *core dynamics* that, in NSE fluids, drive energy cascades and enstrophy intensification.[11,51]

In SE turbulence there are a number of important ramifications implied by the present results:

(a) The mere excitation and propagation of geometry-altering Kelvin waves along the vortices do not modify the spectrum and do not lead to significant interscale energy flux. Energy transfer processes are most effectively measured using the time scale that marks the onset of Kelvin wave collisions—specifically, the moment when smaller waves infiltrate the
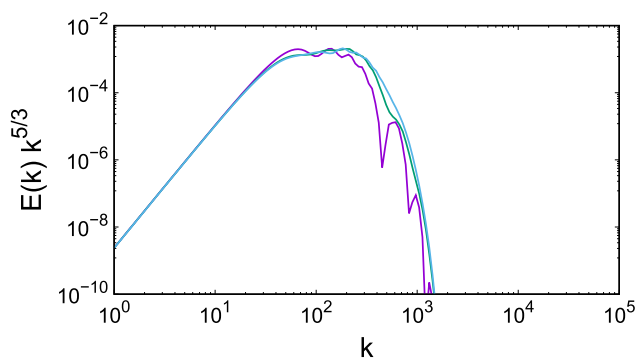
larger Kelvin wave structures and interact with them locally. These interactions are what trigger the energy cascade.

(b) The Kelvin-wave cascade encounters a high wavenumber bottleneck, where a partial statistical equilibration of the accumulated small-scale energy is observed. Meanwhile, some of the cascading energy flux transitions into a $k^{-5/3}$ energy pipeline, primarily generated by interactions between vortices of similar size. These physical processes are related to turbulence dynamics occurring below the intervortex-spacing length scale, which are particularly challenging to resolve in actual turbulence calculations, as a significant portion of the resolution capacity is devoted to discretizing large turbulence scales of system size. Furthermore, the physical processes underlying the $k^{-5/3}$ scaling in SE turbulence are markedly different from those in NSE turbulence, as there is no enstrophy-enhancing vortex stretching present in SE turbulence. Instead, we observe another instance of the success of Kolmogorov's coarse-grained dimensional argument: a local, as indicated by the interaction spectra, energy cascade exhibits a $k^{-5/3}$ scaling when the energy entering the pipeline at low wavenumbers is fully dissipated at the small scales. In algorithmic calculations, the cutoff is determined by numerical damping at the numerical vortex-core scale. In physical processes, we would anticipate that the energy flux reaches scales affected by compressibility and subsequently dissipates into acoustic energy at those scales.

(c) A crucial computational parameter in the vortex dynamical model is the reconnection parameter β, as it governs the reconnection rate. Since reconnections are dissipative processes, they directly influence the rate of energy dissipation within the system. In certain scenarios, such as fully developed turbulence calculations, an excessively high value of β can overdamp the system, resulting in the loss of important physical features, including the high wavenumber bottleneck. One possible way to reduce the arbitrariness of β in a vortex dynamics model is to adopt the approach of Ref. 50, using very fine grids on the vortices that can resolve the microinstabilities leading to vortex reconnections. Although reconnections still occur as discrete events in this method, they happen when the filaments are so close that the arbitrariness is minimal. However, such fine computational grids make fully
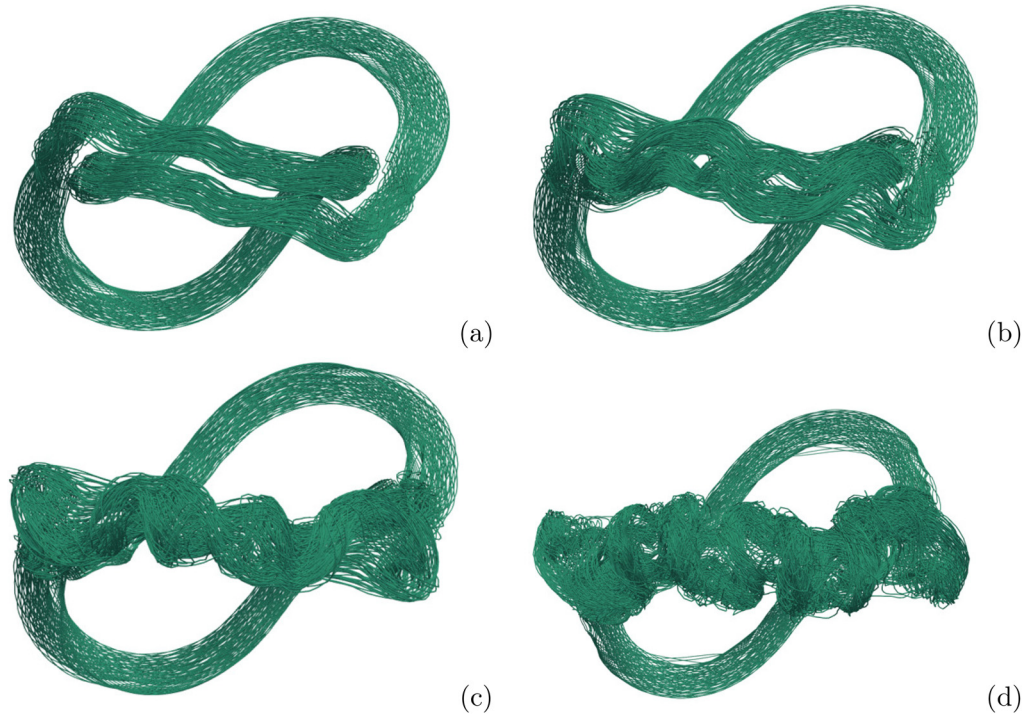

FIG. 38. Bundle link configuration. Compensated energy spectra at times $t = 0$ (purple), $t = 1.0397\tau_c$ (green), and $t = 1.1879\tau_c$ (blue). Initial stages of a $k^{-5/3}$ regime formation.

FIG. 39. Bundle link configuration with augmented circulation. Vortex tangles at $t = 1.0647\tau_c$ (a), $t = 1.1408\tau_c$ (b), $t = 1.2168\tau_c$ (c), and $t = 1.3689\tau_c$ (d).

developed turbulence calculations impractical due to the extremely high computational complexity. The results indicate an alternative practical approach for selecting the reconnection parameter β: begin with a value around $\beta = 0.3$ and gradually decrease it until the physics remain robust against changes in β. In certain cases (though not universally), disabling reconnections may facilitate a clearer observation of a physical effect—such as the bottleneck—that one expects to

capture in reconnecting simulations. Therefore, runs without reconnections could also provide valuable insights for determining the optimal value of β.

In the quantum mechanical interpretation of the Schroedinger equation, the points where the wavefunction is zero correspond to locations where the probability of finding a particle is also zero. Hence, since the line vortices in the Schroedinger equation define the geometry and topology of

FIG. 40. Bundle link configuration with augmented circulation. An enlarged view of the emergent vortex structures generated by the Crow instability at $t = 1.3689\tau_c$.
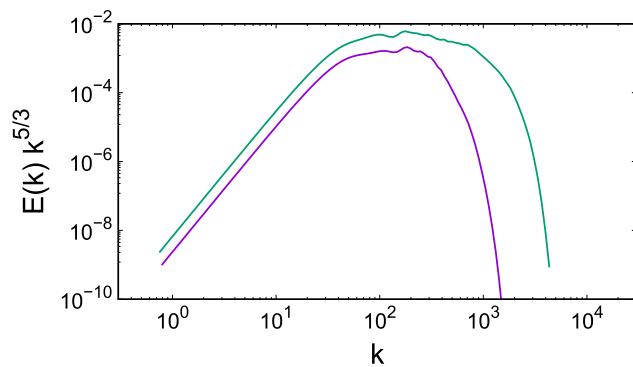
FIG. 41. Bundle link configuration. Comparing the spectra of the 49-ring bundles (purple) and the 81-ring bundles indicates a prominent $k^{-5/3}$ regime in the latter, which is less pronounced in the former. In the 81-ring case, the $k^{-5/3}$ scaling arises from the stretching of the emergent vortex structures induced by the Crow instability.

these zero-probability locations, it would be interesting to investigate which particle motions correspond to "turbulent" quantum probability fields.[3] Moreover, since the vortex dynamical description applies equally well to nonlinear Schroedinger equations, there may be connections between the present results and contemporary nonlinear generalizations of quantum mechanics.[54]

In NSE turbulence there are a number of important ramifications implied by the present results:

(a) The results suggest that Kolmogorov scaling is accurately predicted by dimensional analysis because it reflects the physical reality of large-scale energy flux entering a pipeline and dissipating at smaller scales, regardless of the specific mechanism driving the energy transfer. Indeed, while the self-stretching of large core vortices initiates an energy cascade to smaller scales, further amplified by the stretching of emergent vortex structures spontaneously created by instabilities, the $k^{-5/3}$ scaling only emerges once this iterative process has sufficiently advanced. At this stage, the flow enstrophy is confined within tubular regions where the core size is only a small fraction of the system size, rendering the vortices quasi-singular when viewed on a large scale. In other words, it is these quasi-singular structures at the culmination of the cascade process that dictate the spectrum's scaling, rather than the cascade process itself. In alignment with these conclusions, the Kolmogorov spectrum in the SE is generated by completely different vortex processes, i.e., direct energy-transferring interactions between Kelvin waves along the system's filaments, hence, it reflects the dynamical origins of the energy cascade.

(b) Although vortex stretching during the turbulent cascade involves vortex-core torsion and partial sheetification, these features are not essential for the $k^{-5/3}$ scaling. It seems that the crucial factor is the singular nature of intense enstrophy events combined with their *closed tubular topology*, rather than their internal geometric structure. The internal geometric structure is related to cascade mechanics, as various

processes produce distinct vortex line geometries. Therefore, it is crucial to examine the prevalence of closed tubular vortex topology in fully resolved Navier–Stokes solutions and explore its connection to the Kolmogorov spectrum. This observation clarifies why coarser filament models with simplified core structures can effectively capture key characteristics of vortex stretching and the energy spectrum in turbulent flows.[16]

(c) The $k^{-5/3}$ scaling extends to higher wavenumbers through the formation of emergent vortex structures driven by Crow or helical vortex line instabilities, followed by their self-stretching. This mechanism explains why increased flow inertia results in larger inertial ranges while maintaining the same $k^{-5/3}$ scaling: The initial instabilities create filamentary vortex structures, whose self-stretching drives an energy cascade to smaller scales. Higher inertia means that the initial vortex structures, having high circulation values, will have sufficiently high vortex line densities within their cores. As a result, the emergent vortex structures will also have adequate circulation to self-stretch further and generate even more confined enstrophy structures. This mechanism, which propagates Kolmogorov's scaling to progressively smaller scales, will continue until the available vortex line density for generating new instability-induced vortex structures is depleted. The onset of Kolmogorov's scaling coincides with the formation of structures that appear as quasi-singular events from a large-scale perspective (i.e., "fully developed turbulence"). Greater flow inertia allows for higher vortex line density (larger circulation) within the initially formed filaments, enabling more iterations of this mechanism. Each iteration pushes Kolmogorov's scaling to progressively smaller scales. At large Taylor Reynolds numbers, there would be a range of quasi-singular vortex-core sizes small enough to produce Kolmogorov scaling, with the smallest of these structures setting its high-wavenumber cutoff.

(d) In Richardson's cascade,[8] energy is transferred across scales through the break-up of large eddies into progressively smaller ones. This process is considered continuous, with no gaps between eddy sizes. Although Richardson eddies (often referred to as "swirls") are distinct from vortices, our results, in agreement with other studies,[55,56] support the concept of a continuous energy transfer across scales, consistent with Kolmogorov's postulates. However, they also suggest that Kolmogorov's scaling propagates to higher wavenumbers in a stepwise manner, with jumps from one quasi-singular scale to the next. The size of these jumps is determined by the circulation of the emergent structures, which influences the extent of vortex core reduction.

(e) The emergence of the $k^{-5/3}$ spectrum in the highly ordered vortex configurations of our initial conditions suggests that a random distribution of vorticity is not required for the Kolmogorov spectrum to develop. This is notable given that turbulence is typically associated with randomness and chaos.

(f) The results demonstrate how SE vortex dynamics can be utilized in studying NSE vortices. Given the inviscid nature of SE vortices, the modeled NSE dynamics correspond to high Reynolds number flows.[25] This approach enables the probing

of inertial processes that are challenging to capture with numerical solutions of the NSE. For example, in a related study solving the NSE for the vortex link case at $Re = 4000$,[53] the emergent vortex structures were less pronounced than in our study, hence their impact on flow energetics was not addressed.

ACKNOWLEDGMENTS

AUTHOR DECLARATIONS
Conflict of Interest

The authors have no conflicts to disclose.

Author Contributions

Adrian Parrado Almoguera: Conceptualization (equal); Formal analysis (equal); Investigation (equal); Methodology (equal). **Demosthenes Kivotides:** Conceptualization (equal); Formal analysis (equal); Investigation (equal); Methodology (equal); Supervision (equal); Writing – original draft (equal).

DATA AVAILABILITY

The data that support the findings of this study are available within the article.

REFERENCES

[1] T. Chiueh, T.-P. Woo, H.-Y. Jian, and H.-Y. Schive, "Vortex turbulence in linear Schroedinger wave mechanics," J. Phys. B: At. Mol. Opt. Phys. **44**, 115101 (2011).

[2] J. Koplik and H. Levine, "Vortex reconnection in superfluid helium," Phys. Rev. Lett. **71**, 1375 (1993).

[3] R. E. Wyatt, *Quantum Dynamics with Trajectories: Introduction to Quantum Hydrodynamics* (Springer, Berlin, 2005).

[4] D. Kivotides, "Energy spectra of finite temperature superfluid helium-4 turbulence," Phys. Fluids **26**, 105105 (2014).

[5] A. Chern, F. Knoeppel, U. Pinkall, P. Schroeder, and S. Weissmann, "Schroedinger's smoke," ACM Trans. Graph. **35**, 1 (2016).

[6] S. K. Nemirovskii, "Statistical signature of vortex filaments: Dog or tail? Talk given at QFS," arXiv:1611.09716 (2016).

[7] S. K. Nemirovskii, "Modeling of classical turbulence by quantized vortices," J. Eng. Thermophys. **26**, 476 (2017).

[8] P. Davidson, *Turbulence: An Introduction for Scientists and Engineers* (Oxford University Press, Oxford, 2015).

[9] A. Tsinober, *An Informal Conceptual Introduction to Turbulence* (Springer, Berlin, 2009).

[10] P. G. Saffman, *Vortex Dynamics* (Cambridge University Press, Cambridge, 1993).

[11] A. J. Chorin, *Vorticity and Turbulence* (Springer, Berlin, 1994).

[12] J.-Z. Wu, H.-Y. Ma, and M.-D. Zhou, *Vorticity and Vortex Dynamics* (Springer, Berlin, 2006).

[13] D. I. Pullin and P. G. Saffman, "Vortex dynamics in turbulence," Annu. Rev. Fluid Mech. **30**, 31 (1998).

[14] D. Kuechemann, "Report on the IUTAM Symposium on concentrated vortex motions in fluids," J. Fluid Mech. **21**, 1 (1965).

[15] H. K. Moffatt, S. Kida, and K. Ohkitani, "Stretched vortices - The sinews of turbulence; large-Reynolds-number asymptotics," J. Fluid Mech. **259**, 241 (1994).

[16] D. Kivotides and A. Leonard, "Quantized turbulence physics," Phys. Rev. Lett. **90**, 234503 (2003).

[17] D. Kivotides, "Coherent structure formation in turbulent thermal superfluids," Phys. Rev. Lett. **96**, 175301 (2006).

[18] D. Kivotides, A. J. Mee, and C. F. Barenghi, "Magnetic field generation by coherent turbulence structures," New J. Phys. **9**, 291 (2007).

[19] Y. Dubief and F. Delcayre, "On coherent-vortex identification in turbulence," J. Turbul. **1**, 011 (2000).

[20] M. Carbone and A. D. Bragg, "Is vortex stretching the main cause of the turbulent energy cascade?" J. Fluid Mech. **883**, R2-1 (2020).

[21] P.-F. Yang, Z. D. Zhou, H. Xu, and G. W. He, "Strain self-amplification is larger than vortex stretching due to an invariant relation of filtered velocity gradients," J. Fluid Mech. **955**, A15-1 (2023).

[22] P. L. Johnson, "Energy transfer from large to small scales in turbulence by multi-scale nonlinear strain and vorticity interactions," Phys. Rev. Lett. **124**, 104501 (2020).

[23] A. J. Majda and A. L. Bertozzi, *Vorticity and Incompressible Flow* (Cambridge University Press, Cambridge, 2001).

[24] D. Kivotides, C. F. Barenghi, and D. C. Samuels, "Fractal dimension of superfluid turbulence," Phys. Rev. Lett. **87**, 155301 (2001).

[25] D. Kivotides and A. Leonard, "Helicity spectra and topological dynamics of vortex links at high Reynolds numbers," J. Fluid Mech. **911**, A25 (2021).

[26] R. P. Feynman, "Chapter II application of quantum mechanics to liquid helium," Prog. Low Temp. Phys. **1**, 17 (1955).

[27] G. P. Bewley, M. S. Paoletti, K. R. Sreenivasan, and D. P. Lathrop, "Characterization of reconnecting vortices in superfluid helium," Proc. Natl. Acad. Sci. U. S. A. **105**, 13707–13710 (2008).

[28] B. V. Svistunov, "Superfluid turbulence in the low-temperature limit," Phys. Rev. B **52**, 3647 (1995).

[29] D. Kivotides, J. C. Vassilicos, D. C. Samuels, and C. F. Barenghi, "Kelvin waves cascade in superfluid turbulence," Phys. Rev. Lett. **86**, 3080 (2001).

[30] W. F. Vinen and J. J. Niemela, "Quantum turbulence," J. Low Temp. Phys. **128**, 167 (2002).

[31] S. K. Nemirovskii, "Energy spectrum of the quantum vortices configurations," Low Temp. Phys. **41**, 478 (2015).

[32] D. Kivotides and A. Leonard, "Physics of superfluid helium-4 vortex tangles in normal-fluid strain fields," Phys. Rev. Fluids **6**, 044702 (2021).

[33] R. McKeown, R. Ostilla-Monico, A. Pumir, M. P. Brenner, and S. M. Rubinstein, "Cascade leading to the emergence of small structures in vortex ring collisions," Phys. Rev. Fluids **3**, 124702 (2018).

[34] M. Kiya and H. Ishii, "Vortex interaction and Kolmogorov spectrum," Fluid Dyn. Res. **8**, 73 (1991).

[35] M. J. Wadas, W. J. White, H. J. LeFevre, C. C. Kuranz, A. Towne, and E. Johnsen, "Hydrodynamic mechanism for clumping along the equatorial rings of SN1987A and other stars," Phys. Rev. Lett. **132**, 111201 (2024).

[36] D. Kivotides and L. Wilkin, "Elementary vortex processes in thermal superfluid turbulence," J. Low Temp. Phys. **156**, 163 (2009).

[37] G. S. Winckelmans and A. Leonard, "Contributions to vortex particle methods for the computation of three-dimensional incompressible unsteady flows," J. Comput. Phys. **109**, 247 (1993).

[38] G.-H. Cottet and P. D. Koumoutsakos, *Vortex Methods: Theory and Practice* (Cambridge University Press, Cambridge, 2008).

[39] A. Leonard, "Computing three-dimensional incompressible flows with vortex elements," Annu. Rev. Fluid Mech. **17**, 523 (1985).

[40] R. J. Donnelly, *Quantized Vortices in Helium II* (Cambridge University Press, Cambridge, 1991).

[41] K. W. Schwarz, "Three-dimensional vortex dynamics in superfluid ^4He: Line-line and line-boundary interactions," Phys. Rev. B **31**, 5782 (1985).

[42] T. Wang, R. Yokota, and L. A. Barba, "ExaFMM: A high-performance fast multipole method library with C++ and Python interfaces," J. Open Source Softw. **6**, 3145 (2021).

[43] S. Pfalzner and P. Gibbon, *Many-Body Tree Methods in Physics* (Cambridge University Press, Cambridge, 1996).

[44] O. Yurkina and S. K. Nemirovskii, "Energy spectrum of 3D velocity field generated by ensemble of semi-fractal vortex loops," J. Eng. Thermophys. **31**, 506 (2022).

[45] O. M. Knio and A. F. Ghoniem, "Numerical study of a three-dimensional vortex method," J. Comput. Phys. **86**, 75 (1990).

[46] R. M. Kerr, "Velocity and scaling of collapsing Euler vortices," Phys. Fluids **17**, 075103 (2015).

[47]M. V. Melander and F. Hussain, "Cross-linking of two antiparallel vortex tubes," Phys. Fluids **1**, 633 (1989).

[48]M. V. Melander and F. Hussain, "Core dynamics on a vortex column," Fluid Dyn. Res. **13**, 1 (1994).

[49]D. Kivotides, "Mutual-friction induced instability of normal-fluid vortex tubes in superfluid helium-4," Phys. Lett. A **382**, 1481–1485 (2018).

[50]A. T. A. M. de Waele and R. G. K. M. Aarts, "Route to vortex reconnection," Phys. Rev. Lett. **72**, 482 (1994).

[51]D. Kivotides, "Superfluid helium-4 hydrodynamics with discrete topological defects," Phys. Rev. Fluids **3**, 104701 (2018).

[52]P. Chatelain, D. Kivotides, and A. Leonard, "Reconnection of colliding vortex rings," Phys. Rev. Lett. **90**, 054501 (2003).

[53]J. Yao, W. Shen, Y. Yang, and F. Hussain, "Helicity dynamics in viscous vortex links," J. Fluid Mech. **944**, A41 (2022).

[54]P. Pearle, *Introduction to Dynamical Wave Function Collapse: Realism in Quantum Physics* (Oxford University Press, Oxford, 2024).

[55]G. L. Eyink and H. Aluie, "Localness of energy cascade in hydrodynamic turbulence. I. Smooth coarse graining," Phys. Fluids **21**, 115107 (2009).

[56]H. Aluie and G. L. Eyink, "Localness of energy cascade in hydrodynamic turbulence. II. Sharp spectral filter," Phys. Fluids **21**, 115108 (2009).

11 December 2024 14:46:50